

Structural basis for HCMV Pentamer recognition by antibodies and neuropilin 2

Daniel Wrapp^{1*}, Xiaohua Ye^{2*}, Zhiqiang Ku², Hang Su², Harrison G. Jones¹, Nianshuang Wang¹, Akaash K. Mishra¹, Daniel C. Freed³, Fengsheng Li³, Aimin Tang³, Leike Li², Dabbu Kumar Jaijyan⁴, Hua Zhu⁴, Dai Wang³, Tong-Ming Fu², Ningyan Zhang², Zhiqiang An^{2#}, Jason S. McLellan^{1#}

¹Department of Molecular Biosciences, The University of Texas at Austin, Austin, TX 78712, USA.

²Texas Therapeutics Institute, Brown Foundation Institute of Molecular Medicine, University of Texas Health Service Center at Houston, Houston, TX 77030, USA.

³Merck Research Laboratories, Merck & Co., Inc., Kenilworth, NJ 07033, USA.

⁴Department of Microbiology, Biochemistry and Molecular Genetics, Rutgers New Jersey Medical School, Newark, NJ 07103, USA.

*These authors contributed equally

#Correspondence to zhiqiang.an@uth.tmc.edu (Z.A.) and jmcclellan@austin.utexas.edu (J.S.M.)

ABSTRACT

Human cytomegalovirus (HCMV) encodes for multiple surface glycoproteins and glycoprotein complexes^{1,2}. One of these complexes, the HCMV Pentamer (gH, gL, UL128, UL130 and UL131), mediates tropism to both epithelial and endothelial cells by interacting with the cell surface receptor neuropilin 2 (NRP2)^{3,4}. Despite the critical nature of this interaction, the molecular determinants that govern NRP2 recognition remain unclear. Here we describe the cryo-EM structure of NRP2 bound to the HCMV Pentamer. The high-affinity interaction between these proteins is calcium-dependent and differs from the canonical C-terminal arginine (CendR) binding that NRP2 typically utilizes^{5,6}. The interaction is primarily mediated by NRP2 domains a2 and b2, which interact with UL128 and UL131. We also determine the structures of four human-derived neutralizing antibodies in complex with the HCMV Pentamer to define susceptible epitopes. The two most potent antibodies recognize a novel epitope yet do not compete with NRP2 binding. Collectively, these findings provide a structural basis for HCMV tropism and antibody-mediated neutralization, and serve as a guide for the development of HCMV treatments and vaccines.

1

MAIN TEXT

2 Human cytomegalovirus (HCMV) is a ubiquitous pathogen and congenital infection can cause
3 debilitating and permanent birth defects⁷⁻⁹. Despite the severity of these infections and the prevalence of
4 this pathogen, there are currently no FDA-approved vaccines and therapeutic options are limited¹⁰⁻¹².
5 HCMV is an enveloped, double-stranded DNA virus of the family *Herpesviridae*¹³. The surface of the viral
6 membrane is decorated by several glycoprotein complexes that mediate viral entry and membrane
7 fusion¹⁴⁻¹⁶. One of these complexes is the HCMV Trimer, composed of glycoproteins gH, gL, and gO^{2,17}.
8 The HCMV Trimer mediates tropism for fibroblasts by binding platelet derived growth factor receptor
9 alpha (PDGFR α)^{18,19}. The HCMV Trimer is also capable of mediating infection of a broader variety of cell
10 types by interacting with transforming growth factor beta receptor 3 (TGF β R3)^{4,20}. The other critical
11 tropism-determining complex is the HCMV Pentamer, which is composed of glycoproteins UL128, UL130,
12 UL131, and the same gH and gL proteins that comprise the bulk of the HCMV Trimer^{1,3}. This elongated
13 heteropentamer mediates tropism for endothelial and epithelial cells by binding to neuropilin 2 (NRP2)
14 and triggering the viral fusion protein, gB, to facilitate viral entry into host cells^{4,15,21-23}.

15 Neuropilins 1 and 2 are single-pass transmembrane proteins that are expressed on the surface of
16 neuronal, epithelial, and endothelial cells^{24,25}. Under normal conditions, these proteins function as
17 receptors and co-receptors that engage in numerous physiological processes, including angiogenesis and
18 development of the nervous system^{26,27}. NRP2 is composed of two N-terminal CUB domains (a1 and a2),
19 two F5/8 domains (b1 and b2), a MAM domain, a transmembrane domain, and a C-terminal PDZ domain
20 that is thought to mediate cytoplasmic signaling in response to extracellular stimuli^{28,29}. Perhaps the most
21 thoroughly characterized of these stimuli is vascular endothelial growth factor (VEGF)³⁰. The crystal
22 structure of these proteins in complex with one another has been determined, revealing that the b1
23 domain of NRP2 engages the C-terminal arginine of VEGF^{6,31}. Since this initial characterization, the
24 NRP2 b1 domain has been shown to interact with other binding partners via the same mechanism³²,
25 prompting the moniker “CendR” to refer to this exposed C-terminal arginine motif⁵. Although it has been
26 shown that soluble NRP2 is capable of inhibiting HCMV infection of epithelial cells⁴, the molecular
27 determinants that mediate this interaction remain unclear, and several additional Pentamer receptors
28 have been proposed^{33,34}. The most potently neutralizing HCMV-directed antibodies are elicited against

29 the Pentamer, suggesting that it represents a susceptible target for the development of vaccines and
30 immunotherapeutics³⁵⁻³⁷.

31 To investigate NRP2 and mAb binding, we initiated structural and biophysical studies. Based on
32 previous crystallographic experiments that reported conserved calcium-coordinating loops in both the a1
33 and a2 domains of NRP2^{38,39}, we measured the affinity of recombinantly expressed NRP2 a1a2b1b2 for
34 the soluble HCMV Pentamer ectodomain in both the presence and absence of calcium. We found that in
35 the presence of 2 mM EDTA, no association between NRP2 and Pentamer could be detected. However,
36 when the same experiment was performed in the presence of 2 mM CaCl₂, the affinity of the interaction
37 was determined to be 2.2 nM (**Supplementary Fig. 1a-b**). It is possible that a failure to add additional
38 calcium is what necessitated the use of chemical cross-linkers during previous efforts to observe this
39 complex by negative-stain electron microscopy⁴. The addition of 2 mM CaCl₂ enabled us to form a stable
40 ~230 kDa complex that was suitable for cryo-EM screening. The addition of 0.1% amphipol A8-35 helped
41 to prevent aggregation and allowed for the determination of a 4.0 Å resolution cryo-EM structure of the
42 HCMV Pentamer bound by human NRP2 (**Fig. 1a, Supplementary Figs. 2 and 3**). Performing focused
43 refinement on the NRP2-bound UL proteins yielded a 3.65 Å reconstruction that aided in model building
44 and refinement.

45 These reconstructions revealed an extensive binding interface, with contacts formed by NRP2
46 domains a1, a2 and b2 (**Fig. 1**). Notably, the calcium-coordinating loop of domain a2 (residues 251–258)
47 forms a sizable portion of this binding interface, likely providing an explanation as to why high-affinity
48 NRP2 binding could only be observed after the addition of 2 mM CaCl₂ (**Fig. 1a-b**). Additional contacts
49 are formed between the C-terminal beta strands of ULs 130 and 131 and a loop formed by residues 453–
50 461 of the b2 domain of NRP2 (**Fig. 1c**). This mode of NRP2 binding differs from the canonical CendR
51 motif binding that has been described previously for other NRP2-binding partners^{40,41}. The CendR binding
52 mechanism involves the engagement of a C-terminal arginine residue by the b1 domain, whereas
53 Pentamer is exclusively bound by the a1, a2, and b2 domains. Furthermore, none of the three UL
54 proteins contain a positively charged C-terminal arginine that makes up the CendR motif. As expected,
55 the majority of the binding interface from the Pentamer is composed of the tropism-determining UL
56 proteins, particularly UL128 and UL131^{1,3}, which respectively contribute 437.5 Å² and 208.4 Å² of buried

57 surface area to the interface. Whereas the NRP2 a2, b1, and b2 domains are clustered tightly together at
58 the head of the Pentamer, the N-terminal a1 domain is tethered via a flexible linker that allows it to bind
59 near the middle of the Pentamer, where the C-terminus of UL128 associates with gL. The local resolution
60 for this portion of the reconstruction was relatively poor compared to the rest of the complex, suggesting
61 either conformational flexibility in this region or a loose association of a1. To test the importance of the a1
62 domain, we expressed NRP2 with a 144-residue N-terminal truncation and observed that even in the
63 absence of this flexibly tethered a1 domain, NRP2 a2b1b2 was capable of binding to the HCMV
64 Pentamer with 7.9 nM affinity (**Supplementary Fig. 1c**), supporting our structural observations that the
65 critical determinants of Pentamer binding are contained within NRP2 domains a2b1b2. Intriguingly, our
66 cryo-EM data processing also revealed that a second, more poorly resolved copy of NRP2 could be
67 observed binding near the C-terminal arginine of gL via the b1 domain (**Supplementary Figs. 2 and 4**).
68 Although this second NRP2 appears to exhibit the canonical CendR binding, it could only be observed in
69 ~40% of particles. Furthermore, its binding to the gL protein rather than the tropism-determining UL
70 proteins suggests that this second copy of NRP2 is likely an artifact of the high concentrations of NRP2
71 that were used to form a stable complex. Overall, the conformation of the receptor-bound Pentamer
72 ectodomain does not drastically differ from that of the unbound Pentamer⁴² (**Supplementary Fig. 5**),
73 suggesting that rather than undergoing substantial conformational rearrangements, this complex acts as
74 a tether to connect HCMV virions to the surface of epithelial and endothelial cells until the viral fusogen
75 gB fuses the viral and cellular membranes.

76 Previous efforts to characterize the humoral immune response to asymptomatic HCMV infection
77 yielded an extensive panel of neutralizing antibodies directed against gB, the HCMV Trimer, and the
78 HCMV Pentamer^{35,43,44}. To learn more about the mechanisms of neutralization of high-affinity, Pentamer-
79 directed antibodies, we determined cryo-EM structures of four naturally elicited human antibodies in
80 complex with the Pentamer (**Fig. 2, Supplementary Figs. 3, 6, 7, and 8**). The flexibility and elongated
81 shape of the Pentamer necessitated focused refinements of the Fabs along with the domains making up
82 their respective epitopes. Model building was facilitated by high-resolution crystal structures of unbound
83 Fabs (1-103: 1.9 Å, 1-32: 2.1 Å, 2-18: 2.8 Å, 2-25: 2.5 Å), which were then used as reference restraints
84 and lightly refined as a part of the complex (**Supplementary Tables 1 and 2**). Three of these antibodies

85 (1-103, 2-18, and 2-25) bound solely to the UL proteins at the head of the Pentamer, whereas the fourth
86 (1-32) bound to gL, near the junction between the UL proteins and the conserved gH/gL scaffold (**Fig.**
87 **2a**). The Fab 1-103 epitope is solely composed of residues from the membrane-distal tip of UL128,
88 sometimes referred to as Site 1 of immunogenic region (IR) ^{14,35}. The epitopes of Fabs 2-18 and 2-25
89 overlap substantially, with both Fabs binding to the junction between ULs 128 and 131. This junction
90 where UL128 meets UL131 does not fit into one of the preexisting antigenic sites, but rather overlaps with
91 both Site 2 and Site 5 of IR^{14,35}. The Fab 1-32 epitope spans the interface between gH and gL, slightly
92 below Site 4/6 in IR^{24,35} (**Fig. 2b**). This epitope is consistent with previous observations³⁵ that 1-32 is the
93 only one of the four antibodies evaluated that was capable of binding to both the fully assembled HCMV
94 Pentamer and disulfide-linked homodimers of the gH/gL heterodimer. Despite the ability to recognize the
95 gH/gL heterodimer that serves as the scaffold for assembly of both the HCMV Pentamer and Trimer, 1-32
96 was only capable of neutralizing HCMV infection in epithelial cells³⁵.

97 By analyzing the structures of these immunocomplexes in conjunction with the structure of
98 Pentamer bound by NRP2, it becomes possible to delineate more clearly the molecular basis for
99 neutralization (**Fig. 3**). The CDR H3 and CDR L1 of Fab 1-103 compete with NRP2 by binding to the
100 same portion of Pentamer that is engaged by the calcium-coordinating loop (residues 251 to 258) of
101 NRP2 domain a2. By binding to the junction between gL and the UL head of Pentamer, Fab 1-32
102 occupies the same space as several of the loops of the a1 domain of NRP2 (residues 45–48; 72–77;
103 106–110) via its CDR L1 (**Fig. 3b**). Consistent with the relatively poor density for domain a1, we found
104 that when bound by 1-32, Pentamer was still capable of interacting with NRP2, albeit with diminished
105 affinity (133 nM) (**Supplementary Fig. 9**), further supporting our findings that the a1 domain is not strictly
106 required for binding to Pentamer. This observation is also consistent with the relatively weak
107 neutralization capacity of 1-32 compared to 1-103, which competes for the a2b1b2 interface.

108 Intriguingly, the two most potently neutralizing mAbs that we examined, 2-18 and 2-25 (**Fig. 4a**),
109 do not appear to compete with NRP2 a1a2b1b2 based on our structural analysis. Furthermore, although it
110 is possible that 2-18 and 2-25 compete with the C-terminal MAM domain, this seems unlikely based on
111 the position of the C-terminus of b2⁴⁵. These mAbs are both directed against an epitope at the junction
112 between ULs 128 and 131, and although this epitope is directly adjacent to the NRP2 binding interface,

113 the binding angles of 2-18 and 2-25 result in these two Fabs being directed away from the β -sheet-rich
114 face of the Pentamer that is responsible for engaging NRP2. A biolayer interferometry-based competition
115 assay confirmed our structural observation that Fabs 2-18 and 2-25 do not disrupt the interaction between
116 Pentamer and NRP2 a1a2b1b2 (**Fig. 4b**). These two Fabs are still capable of neutralizing HCMV *in vitro*
117 even when administered up to 30 minutes after allowing viruses to adhere to human epithelial cells,
118 although we observed a significant decrease in the neutralization potency of 2-25 Fab, as compared to 2-
119 25 IgG (**Figs. 4a, 4c**). This broad and potent neutralization of multiple HCMV strains (**Fig. 4d**), which
120 occurs without disrupting the interaction between NRP2 a1a2b1b2 and the Pentamer, suggests that 2-18
121 and 2-25 neutralize via a distinct mechanism from 1-103 and 1-32 (**Supplementary Fig. 10**). Whether 2-
122 18 and 2-25 prevent the association of an unidentified secondary receptor or prevent some
123 conformational change that is required to trigger gB-induced membrane fusion remains unclear and
124 requires additional investigation.

125 Collectively, these data provide a molecular basis of HCMV tropism for both epithelial and
126 endothelial cells. Due to the importance of these cell types during natural infection, this represents a
127 critical advance in our understanding of how HCMV engages host cells at one of the earliest stages of
128 infection^{22,46}. Similarly, the structure of the HCMV Trimer was recently reported in complex with PDGFR α
129 and TGF β R3, two host cell receptors that both mediate tropism of fibroblasts^{18,20}. In an effort to explain
130 how this interaction might lead to triggering of gB and viral fusion, the authors speculate that receptor
131 engagement of the Trimer may induce a rigid-body rotation relative to the viral membrane that causes the
132 attachment complex to destabilize prefusion gB⁴⁷. Our findings agree with their observation that receptor
133 binding does not induce any conformation changes, lending credence to the hypothesis that a rigid-body
134 rotation of the receptor-binding complex may act as trigger to induce membrane fusion. However, the
135 existence of neutralizing mAbs that do not disrupt NRP2 binding suggests that additional fusion triggers,
136 perhaps in the form of secondary receptors^{33,34} may exist, necessitating further investigation.

137 In addition to detailing the molecular determinants that mediate HCMV infection, these findings
138 expand our understanding of how antibody-mediated neutralization of HCMV can be achieved. Previous
139 structural work has delineated a series of antigenic sites covering the surface of the Pentamer^{4,35,42,48}, but
140 in the absence of high-resolution information regarding the NRP2 binding interface, the mechanisms of

141 neutralization for antibodies targeting these sites were unknown. Our data suggest that it may be possible
142 to neutralize HCMV via multiple, distinct mechanisms simultaneously by administering a cocktail of
143 Pentamer-directed antibodies^{36,49,50}. By elucidating which epitopes on the surface of the Pentamer are
144 susceptible to antibody-mediated neutralization, these findings will also help to guide future structure-
145 based vaccine design efforts.

146

147

ACKNOWLEDGEMENTS

148

We thank Emilie Shipman and Dr. John Ludes-Meyers for their assistance with cell transfection and protein production; Drs. Aguang Dai and Sasha Dickinson at the Sauer Structural Biology Laboratory for their assistance with microscope alignment and data collection; the 19-ID beamline staff at the Structural Biology Center at the Advanced Photon Source, Argonne National Laboratory; and Dr. Georgina Salazar for assistance with manuscript preparation. This study was funded in part by grants from Merck & Co., Inc. Kenilworth, NJ, USA, the Texas Emerging Technology Fund, and the Welch Foundation Grant No. AU-0042-20030616. The Sauer Structural Biology Laboratory is supported by the University of Texas College of Natural Sciences and by award RR160023 from the Cancer Prevention and Research Institute of Texas (CPRIT). Argonne National Laboratory is operated by UChicago Argonne, LLC, for the U.S. Department of Energy (DOE), Office of Biological and Environmental Research under Contract DE-AC02-06CH11357.

158

AUTHOR CONTRIBUTIONS

159

D.W., X.Y., Z.A., and J.S.M. conceived of and designed experiments. D.W., X.Y., H.G.J., N.W., and A.K.M. produced and purified proteins. D.W., H.G.J., and A.K.M. performed crystallographic studies. D.W. performed BLI and SPR experiments. D.W. and J.S.M. collected and analyzed cryo-EM data. X.Y., Z.K., and L.L. established the neutralization assays and X.Y., H.S., D.C.F., and F.L. performed the assays. X.Y., Z.K., A.T., and D. Wang analyzed the neutralization data. D.K.J. and H.Z. prepared the HCMV AD169rev-GFP virus. Z.A., T-M.F., N.Z., and J.S.M. supervised experiments. D.W., X.Y., Z.A., and J.S.M. wrote the manuscript with input from all authors.

166

167

DECLARATIONS OF INTEREST

168

169

Z.A. and T-M.F. have filed a patent related to the antibody 2-18. D.C.F., F.L., A.T., and D. Wang are Merck & Co., Inc. employees. Other authors declare no competing interests.

170

171

FIGURE LEGENDS

172 **Figure 1:** The cryo-EM structure of the HCMV Pentamer bound by NRP2. (a) Cryo-EM density is shown
173 (*left*), with the Pentamer colored in shades of green, gray and white and NRP2 colored orange. The
174 atomic model of this complex (*right*) is shown as ribbons, with the NRP2 also represented by a
175 transparent molecular surface. (b) The interface between the NRP2 a2 domain and UL128. UL128 is
176 depicted as a transparent, green molecular surface with ribbons underneath and NRP2 is shown as
177 orange ribbons. Residues that are predicted to form critical contacts are shown as sticks. Oxygen,
178 nitrogen, and sulfur atoms are colored red, blue, and yellow, respectively. The single calcium atom is
179 shown as a bright green sphere, with black dotted lines depicting the interaction with conserved
180 coordinating residues. (c) The interface between the NRP2 b2 domain and the HCMV Pentamer. ULs 130
181 and 131 are shown as a transparent, green molecular surface and NRP2 is shown as orange ribbons,
182 with residues predicted to form critical contacts shown as sticks. Oxygen and nitrogen atoms are colored
183 red and blue, respectively.

184

185 **Figure 2:** Composite of cryo-EM structures of Pentamer bound by four neutralizing human antibodies. (a)
186 The atomic models of two cryo-EM structures of antibodies bound to the HCMV Pentamer are
187 superimposed based on the position of the UL proteins. The Pentamer is shown as a molecular surface,
188 colored according to **Fig. 1** and Fabs are shown as ribbons surrounded by a transparent molecular
189 surface. Fab 1-103 is colored blue, Fab 1-32 is colored gold, Fab 2-18 is colored purple and Fab 2-25 is
190 colored red. (b) CDRs from each Fab are shown as ribbons and the Pentamer is shown as a transparent,
191 molecular surface with ribbons underneath. Predicted critical contact residues are shown as sticks. Fab 1-
192 103 (*top left*) is colored blue, Fab 1-32 (*bottom left*) is colored gold, Fab 2-18 (*top right*) is colored purple
193 and Fab 2-25 (*bottom right*) is colored red. Oxygen, nitrogen and sulfur atoms are colored red, blue and
194 yellow respectively.

195

196 **Figure 3:** Pentamer-directed antibodies can neutralize HCMV via multiple mechanisms. (a) Cryo-EM
197 structures of NRP2-bound Pentamer and Fab-bound Pentamer are superimposed based on the position
198 of the UL proteins. Pentamer is shown as a molecular surface colored according to **Fig. 1**, Fabs are

199 shown as ribbons, colored according to **Fig. 2**, and NRP2 is shown as orange ribbons surrounded by a
200 transparent molecular surface. **(b)** Close-up views of each Fab-bound Pentamer are superimposed upon
201 the NRP2-bound Pentamer. Both Fabs and NRP2 are shown as ribbons surrounded by a transparent
202 molecular surface, while the Pentamer is shown as a solid molecular surface. NRP2 is colored orange, 1-
203 103 is colored blue, 1-32 is colored gold, 2-18 is colored purple and 2-25 is colored red.

204

205 **Figure 4:** Antibodies 2-18 and 2-25 potently neutralize HCMV without disrupting NRP2 binding. **(a)**
206 Neutralization curves are shown for each mAb based on inhibition of AD169rev-GFP infection in ARPE-
207 19 cells. Inhibitory curves for both IgG and Fab are shown, with IgG shown in darker colors. **(b)**
208 Sensorgrams from a BLI-based competition experiment are displayed. NRP2 was immobilized to a BLI
209 sensor and dipped into Pentamer alone or Pentamer incubated with a molar excess of indicated Fab. **(c)**
210 IgG neutralization of HCMV post-attachment to epithelial cells. AD169rev-GFP virions were allowed to
211 adhere to ARPE-19 cells and saturating concentrations of IgG were added after a variety of different
212 incubation periods. Viral inhibition is plotted for each IgG after either 0 mins incubation, 30 mins
213 incubation, or 60 mins incubation. **(d)** Neutralization potency of 2-18 IgG was evaluated against twelve
214 clinical isolates and two laboratory-adapted HCMV strains in ARPE-19 cells. IC₅₀ values were calculated
215 by non-linear fit of the percentage of viral inhibition vs. concentration (ng/mL). The neutralization results of
216 mAbs 1-103, 1-32 and 2-25 against the same panel of HCMV strains have been reported previously³⁵.

217

218 **Supplementary Figure 1:** The interaction between NRP2 and Pentamer is calcium-dependent. **(a)** BLI
219 sensorgram showing the absence of binding between Pentamer and NRP2 in the presence of 2 mM
220 EDTA. **(b)** BLI sensorgram showing binding between Pentamer and NRP2 in the presence of 2 mM
221 calcium. Data are shown as black lines and best fit of a 1:1 binding model is shown as red lines. **(c)** BLI
222 sensorgram showing binding between Pentamer and NRP2 a2b1b2 in the presence of 2 mM calcium.
223 Data are shown as black lines and best fit of a 1:1 binding model is shown as red lines.

224

225 **Supplementary Figure 2:** Pentamer + NRP2 cryo-EM data processing workflow.

226

227 **Supplementary Figure 3:** Cryo-EM structure validation. **(a)** FSC curves are shown for focused
228 refinements of Pentamer bound by NRP2 (*left*), Pentamer bound by 1-103, 1-32 and 2-25 (*middle*) and
229 Pentamer bound by 2-18 and 8I21 (*right*). **(b)** Cryo-EM maps from each focused refinement are shown,
230 colored according to local resolution. **(c)** Portions of each cryo-EM map are shown, with the
231 corresponding atomic models docked into the density. Residue numbering corresponds to UL130 (*left*,
232 *middle*) and UL131 (*right*). **(d)** Viewing Direction Distribution charts from cryoSPARC are shown for each
233 focused refinement.

234

235 **Supplementary Figure 4:** A subset of particles display a second copy of NRP2 bound to the C-terminus
236 of gL. **(a)** Two-dimensional class averages of Pentamer bound by two copies of NRP2 are shown. **(b)** A
237 ~4.2 Å cryo-EM reconstruction of Pentamer bound by two copies of NRP2 is shown as a transparent
238 surface. Atomic models of each component are docked in, shown as ribbons. Both copies of NRP2 are
239 colored orange and Pentamer is colored white, except for gL, which is colored blue-to-red from the N-
240 terminus to the C-terminus. The a1 domain from the gL-bound copy of NRP2 was excluded because it
241 could not clearly be resolved in this reconstruction.

242

243 **Supplementary Figure 5:** NRP2 binding does not alter the conformation of Pentamer. **(a)** Previously
244 reported crystal structures of Pentamer⁴² (PDB IDs: 5V0B and 5V0D) are aligned to the cryo-EM structure
245 of the NRP2-bound Pentamer, based on the position of gH. 5V0B is colored blue, 5V0D is colored red
246 and NRP2-bound Pentamer is colored yellow. **(b)** A previously reported crystal structure of NRP2³⁸ (PDB
247 ID: 2QQK) is aligned to the cryo-EM structure of Pentamer-bound NRP2, based on the position of the b1
248 domain. 2QQK is colored purple and Pentamer-bound NRP2 is colored orange.

249

250 **Supplementary Figure 6:** Pentamer + 1-103 + 1-32 + 2-25 cryo-EM data processing workflow.

251

252 **Supplementary Figure 7:** Pentamer + 2-18 + 8I21 cryo-EM data processing workflow.

253

254 **Supplementary Figure 8:** Binding kinetics of Pentamer-directed antibodies. SPR sensorgrams showing
255 binding of each of the four neutralizing Fabs are displayed, with data shown as black lines and the best fit
256 of a 1:1 binding model shown as red lines.

257

258 **Supplementary Figure 9:** NRP2 binding to Pentamer is partially disrupted by the presence of 1-32.
259 Sensorgrams are shown for an experiment in which 1-32 IgG was immobilized to a BLI sensor, then used
260 to capture Pentamer before being dipped into NRP2. Data for the association and dissociation of NRP2
261 are shown as black lines and the lines of best fit of a 1:1 binding model are shown as red lines.

262

263 **Supplementary Figure 10:** Pentamer-directed mAbs neutralize via distinct mechanisms. A cartoon is
264 shown depicting the infection of an endothelial or epithelial cell by HCMV. Pentamer is colored according
265 to **Fig. 1**, NRP2 is colored orange and the three protomers of gB are colored red, blue and yellow. The
266 stages of infection that mAbs 1-103, 1-32, 2-18 and 2-25 are predicted to disrupt are denoted by inhibition
267 arrows.

268

269 **Supplementary Table 1:** X-ray crystallographic data collection and refinement.

270

271 **Supplementary Table 2:** Cryo-EM data collection and refinement.

272

273

274

275
276
277

METHODS

Protein production and purification

278 Plasmids encoding the heavy and light chains of 1-103, 1-32, 2-18, 2-25 and 8I21 IgG with an
279 HRV3C protease cleavage site engineered into the hinge between the CH1 and CH2 domains of the
280 heavy chain were co-transfected into FreeStyle 293F cells using polyethylenimine. To produce the
281 soluble ectodomain of the HCMV Pentamer (strain Towne), plasmids encoding residues 24-718 of gH
282 with a C-terminal 6x HisTag, residues 31-278 of gL, residues 21-171 of UL128, residues 26-214 of UL130
283 and residues 19-129 of UL131, all with artificial signal sequences were simultaneously co-transfected at
284 an equimolar ratio.

285 Similarly, plasmids encoding an artificial signal peptide, residues 23-595 of human NRP2 and a
286 C-terminal HRV3C cleavage site with either an 8x HisTag and a TwinStrepTag or a monomeric IgG1 Fc
287 tag and an 8x HisTag were transfected into FreeStyle 293F cells, as described above. An N-terminal
288 truncation of NRP2 that encompassed residues 145-595 with an artificial signal sequence and a C-
289 terminal HRV3C cleavage site with a monomeric IgG1 Fc tag and an 8x HisTag (NRP2 a2b1b2) was
290 transfected using the same conditions. NRP2 and NRP2 a2b1b2 were purified from cell supernatants
291 using either StrepTactin resin (IBA) or Protein A resin before being run over a Superdex 200 Increase
292 column using a buffer composed of 2 mM Tris pH 8.0, 200 mM NaCl, 0.02% NaN₃ and 2 mM CaCl₂.

293 To form the complex of Pentamer + 1-103 + 1-32 + 2-25, purified 1-103 IgG was immobilized to
294 Protein A resin and this 1-103 resin was then used to capture Pentamer from co-transfected cell
295 supernatants. The 1-103 + Pentamer complex was then eluted by incubation with HRV3C protease and
296 purified over a Superose 6 Increase column in 2 mM Tris pH 8.0, 200 mM NaCl and 0.02% NaN₃. This
297 complex was then passed over a column containing 2-25 IgG immobilized to Protein A resin. Again, the
298 complex was eluted by incubation with HRV3C protease and a molar excess of 1-32 Fab was added
299 before a final round of purification over a Superose 6 Increase column using the same buffer.

300 To form the Pentamer + 2-18 + 8I21 complex, purified 2-18 IgG was immobilized to Protein A
301 resin and used to capture Pentamer from co-transfected cell supernatants. The 2-18 + Pentamer complex
302 was then eluted by incubation with HRV3C protease and mixed with a molar excess of 8I21 Fab before
303 being run over a Superose 6 Increase column in 2 mM Tris pH 8.0, 200 mM NaCl and 0.02% NaN₃.

304 To form the Pentamer + NRP2 complex, purified Pentamer was mixed with a threefold molar
305 excess of 8x His/TwinStrep-tagged NRP2 in a buffer composed of 2 mM Tris pH 8.0, 200 mM NaCl,
306 0.02% NaN₃ and 2 mM CaCl₂ and the two components were allowed to bind on ice for 1 hour. This
307 mixture was then purified over a Superose 6 Increase column (Cytiva) using the same buffer.

308

309 *X-ray crystallographic studies*

310 Purified IgGs 1-103, 1-32, 2-18 and 2-25 were incubated with 10% (wt/wt) His-tagged HRV3C
311 protease on ice for 2 hours before being passed over Protein A and NiNTA resin to removed cleaved Fc
312 and excess protease. The remaining Fab was purified by SEC using a Superdex 200 Increase column in
313 2 mM Tris pH 8.0, 200 mM NaCl and 0.02% NaN₃ (1-132 and 2-18) or 2 mM Tris pH 8.0, 50 mM NaCl
314 and 0.02% NaN₃ (1-103 and 2-25).

315 1-103 Fab was concentrated to 15.00 mg/mL and used to prepare sitting-drop crystallization
316 trays. Diffraction-quality crystals grew in a mother liquor composed of 2.1 M sodium formate, 25% PEG
317 3350, 0.1 M sodium acetate pH 4.5 and 0.1 M calcium chloride. 1-103 Fab crystals were cryoprotected
318 using mother liquor supplemented with 20% glycerol before being plunge frozen into liquid nitrogen.

319 1-32 Fab was concentrated to 11.00 mg/mL and used to prepare hanging-drop crystallization
320 trays. Diffraction-quality crystals were grown in 2.0 M ammonium sulfate, 0.2 M sodium chloride and 5%
321 isopropanol. 1-32 Fab crystals were cryoprotected using mother liquor supplemented with 20% glycerol
322 before being plunge frozen into liquid nitrogen.

323 2-18 Fab was concentrated to 12.00 mg/mL and used to prepare sitting-drop crystallization trays.
324 Small crystalline needles, grown in 0.1 M HEPES pH 7.5 and 45% PEG 400 were used to perform
325 microseed matrix screening, ultimately yielding diffraction-quality crystals in a mother liquor composed of
326 0.2 M ammonium acetate, 0.1 M sodium citrate tribasic dihydrate pH 5.6 and 30% PEG 4000. 2-18 Fab
327 crystals were cryoprotected using mother liquor supplemented with 20% glycerol before being plunge
328 frozen into liquid nitrogen.

329 2-25 Fab was concentrated to 15.4 mg/mL and used to prepare sitting-drop crystallization trays.
330 Diffraction-quality crystals were grown in 30% PEG 4000, a mixture of 0.2 M divalent cations⁵¹ and 0.1 M

331 BIS-TRIS pH 6.5. 2-25 Fab crystals were looped without cryoprotectant and directly plunge frozen into
332 liquid nitrogen.

333 All diffraction data were collected at Argonne National Labs, Advanced Photon Source, SBC-
334 19ID. Datasets were indexed in iMOSFLM⁵² and scaled in AIMLESS⁵³. Molecular replacement solutions
335 were determined using PhaserMR⁵⁴ and models were iteratively built and refined using Coot⁵⁵, PHENIX⁵⁶
336 and ISOLDE⁵⁷. Full crystallographic data collection and refinement statistics can be found in
337 **Supplementary Table 1**. Crystallographic software packages were curated by SBGrid⁵⁸.

338

339 *Cryo-EM sample preparation and data collection*

340 Purified HCMV Pentamer + 2-18 + 8I21 complex was diluted to a concentration of 0.25 mg/mL in
341 2 mM Tris pH 8.0, 200 mM NaCl, 0.02% NaN₃ and 0.01% amphipol A8-35. 8I21 Fab was added after initial
342 attempts to visualize the Pentamer + 2-18 complex were hampered by a lack of distinguishable features
343 (data not shown). 3 μ L of the ternary complex was deposited on a CF-1.2/1.3 grid that was glow discharged
344 at 25 mA for 1 minute using an Emitech K100X (Quorum Technologies). Excess liquid was blotted away
345 for 6 seconds in a Vitrobot Mark IV (FEI) operating at 4° C and 100% humidity before being plunge frozen
346 into liquid ethane. Data were collected on a Titan Krios (FEI) operating at 300 kV, equipped with a K3 direct
347 electron detector (Gatan). Movies were collected using SerialEM⁵⁹ at 22,500x magnification, corresponding
348 to a pixel size of 1.047 Å.

349 Purified HCMV Pentamer + 1-103 + 1-32 + 2-25 complex was diluted to a concentration of 0.2
350 mg/mL in 2 mM Tris pH 8.0, 400 mM NaCl, 0.02% NaN₃ and 0.01% amphipol A8-35. 3 μ L of protein was
351 deposited on a CF-1.2/1.3 grid that was plasma cleaned at 25 mA for 30 seconds using a Solarus plasma
352 cleaner (Gatan). Excess liquid was blotted away for 6 seconds in a Vitrobot Mark IV (FEI) operating at 4°
353 C and 100% humidity before being plunge frozen into liquid ethane. Data were collected on a Titan Krios
354 (FEI) operating at 300 kV, equipped with a K2 direct electron detector (Gatan). Movies were collected using
355 Leginon⁶⁰ at 22,500x magnification, corresponding to a pixel size of 1.075 Å.

356 Purified HCMV Pentamer + NRP2 complex was diluted to a concentration of 0.4 mg/mL in 2 mM
357 Tris pH 8.0, 200 mM NaCl, 2 mM CaCl₂, 0.02% NaN₃ and 0.01% amphipol A8-35. 3 μ L of protein was
358 deposited on an UltrAuFoil 1.2/1.3 grid that was plasma cleaned at 25 mA for 2 minutes using a Solarus

359 plasma cleaner (Gatan). Excess liquid was blotted away for 3 seconds in a Vitrobot Mark IV (FEI) operating
360 at 4° C and 100% humidity before being plunge frozen into liquid ethane. Data were collected on a Titan
361 Krios (FEI) operating at 300 kV, equipped with a K3 direct electron detector (Gatan). Movies were collected
362 using SerialEM⁵⁹ at 22,500x magnification, corresponding to a pixel size of 1.073 Å.

363

364 *Cryo-EM data processing and model building*

365 Motion correction, CTF-estimation and non-templated particle picking using BoxNet were
366 performed in Warp⁶¹. Extracted particles were imported into cryoSPARC⁶² for 2D classification, *ab initio*
367 3D reconstruction calculation, 3D classification and non-uniform refinement⁶³. Based on the flexibility of
368 the interface between the gH/gL and UL proteins, particle subtraction and focused refinement were also
369 performed in cryoSPARC. Final reconstructions were sharpened with DeepEMhancer⁶⁴. A full description
370 of the cryo-EM data processing workflows can be found in **Supplementary Figs. 2, 6 and 7**. Crystal
371 structures were docked into cryo-EM density maps using Chimera⁶⁵ before being refined in Coot⁵⁵,
372 PHENIX⁵⁶ and ISOLDE⁵⁷. A detailed description of the cryo-EM data processing workflow can be found in
373 **Supplementary Figs. 2, 6 and 7**. Full cryo-EM data collection and refinement statistics can be found in
374 **Supplementary Table 2**.

375

376 *Surface plasmon resonance (SPR)*

377 Purified His-tagged Pentamer was immobilized to a single flow cell of a NiNTA sensor in a
378 Biacore X100 (GE Healthcare) to a level of ~800 response units (RUs) using HBS-P+ buffer adjusted to a
379 pH of 8.0. Two-fold serial dilutions of Fabs 1-103, 1-32, 2-18 and 2-25 were injected over both flow cells
380 to measure binding kinetics. The sensor was doubly regenerated using 350 mM EDTA and 100 mM
381 NaOH in between cycles. Data were double reference-subtracted and fit to a 1:1 binding model using
382 Biacore Evaluation Software (GE Healthcare).

383

384 *Biolayer Interferometry (BLI)*

385 Purified monoFc-tagged NRP2 or NRP2 a2b1b2 was immobilized to anti-human capture (AHC)
386 tips (ForteBio) in a buffer composed of 10 mM HEPES pH 8.0, 150 mM NaCl, 0.05% Tween 20, 1 mg/mL

387 BSA and 2 mM CaCl₂. Sensors were then dipped into wells containing purified HCMV Pentamer, ranging
388 in concentration from 50 nM to 3.125 nM. Data were reference subtracted and processed using Octet
389 Data Analysis software v10.0 (ForteBio) with a 1:1 binding model. To evaluate the impact of calcium on
390 Pentamer binding, the same experiment was performed using monoFc-tagged NRP2 in a buffer
391 composed of 10 mM HEPES pH 8.0, 150 mM NaCl, 0.05% Tween 20, 1 mg/mL BSA and 2 mM EDTA.

392 To evaluate competition between Fabs and NRP2, monoFc-tagged NRP2 was immobilized to
393 AHC tips in a buffer composed of 10 mM HEPES pH 8.0, 150 mM NaCl, 0.05% Tween 20, 1 mg/mL BSA
394 and 2 mM CaCl₂. Sensors were then dipped into wells containing a mixture of purified HCMV Pentamer at
395 a concentration of 50 nM and 100 nM Fab. Data were reference subtracted using Octet Data Analysis
396 software v10.0.

397 To measure the binding kinetics of NRP2 to Pentamer in the presence of mAb 1-32, 1-32 IgG
398 was immobilized to AHC sensors using a buffer composed of 10 mM HEPES pH 8.0, 150 mM NaCl,
399 0.05% Tween 20, 1 mg/mL BSA and 2 mM CaCl₂. Tips with immobilized 1-32 were then dipped into wells
400 containing 100 nM Pentamer. The 1-32-captured Pentamer was then dipped into wells containing
401 untagged NRP2, ranging in concentration from 400 nM to 25 nM. Data were reference subtracted and
402 processed using Octet Data Analysis software v10.0 with a 1:1 binding model.

403

404 *HCMV neutralization assay*

405 All of the Pentamer-specific antibodies used for the purposes of neutralization and inhibition assays
406 were produced as described previously⁴³. A dengue virus specific human IgG1 antibody⁶⁶ was used as
407 isotype control. Fabs for neutralization and inhibition assays were generated by digesting IgG with papain
408 (Sigma, P4762) and purifying as described previously⁶⁷. A standard neutralization assay with the Towne-
409 ts15-rR, AD169rev, and 12 clinical isolates as shown in **Supplementary Fig. 10** were performed in ARPE-
410 19 cells using an immunostaining method⁶⁸. Neutralization assays in **Fig. 4** were performed in ARPE-19
411 cells using AD169rev-GFP strain and virus infection was examined through GFP expression as described
412 previously⁶⁹. For the standard neutralization assay, 50 µL/well of AD169rev-GFP, generating about 100
413 GFP-positive cells was incubated with 50 µL/well of serial 2-fold diluted IgG or Fab (at indicated
414 concentrations) at 37 °C for 30 min and then added to confluent ARPE-19 cells grown in a 96-well plate.

415 Mock-infected cells and cells infected with virus-only served as controls. For the post-attachment assay,
416 ARPE-19 cells grown in a 96-well plate were pre-cooled at 4 °C for 10 min. 50 µL/well of AD169rev-GFP
417 was allowed to attach to cells for 1 h at 4 °C. After removing unattached virus through a single wash using
418 cold media, the indicated IgG, diluted at concentrations of ~200 times of corresponding IC₅₀ was added
419 after culturing AD169rev-GFP-attached cells for different lengths of time (0 min, 30 min, and 60 min) in a
420 37 °C incubator. The antibody-containing media was replaced with fresh media without antibody 2 h later.
421 Mock-infected cells and cells infected with virus but not treated with antibodies served as controls. For all
422 above assays, triplicate wells were determined for each condition and viral infection was examined at 48 h
423 post-infection. A C.T.L. Immunospot analyzer was used to capture whole-well images of GFP expression
424 and quantification of GFP-positive cells. The percentage of viral inhibition by the antibody and the IC₅₀ of
425 each antibody was calculated by non-linear fit of virus inhibition % vs. concentration (ng/mL) using
426 GraphPad Prism® 5 software.

427

428
429

REFERENCES

430 1 Gerna, G. *et al.* Dendritic-cell infection by human cytomegalovirus is restricted to strains
431 carrying functional UL131-128 genes and mediates efficient viral antigen presentation to
432 CD8+ T cells. *J Gen Virol* **86**, 275-284, doi:10.1099/vir.0.80474-0 (2005).

433 2 Vanarsdall, A. L., Chase, M. C. & Johnson, D. C. Human cytomegalovirus glycoprotein gO
434 complexes with gH/gL, promoting interference with viral entry into human fibroblasts
435 but not entry into epithelial cells. *J Virol* **85**, 11638-11645, doi:10.1128/JVI.05659-11
436 (2011).

437 3 Adler, B. *et al.* Role of human cytomegalovirus UL131A in cell type-specific virus entry
438 and release. *J Gen Virol* **87**, 2451-2460, doi:10.1099/vir.0.81921-0 (2006).

439 4 Martinez-Martin, N. *et al.* An Unbiased Screen for Human Cytomegalovirus Identifies
440 Neuropilin-2 as a Central Viral Receptor. *Cell* **174**, 1158-1171 e1119,
441 doi:10.1016/j.cell.2018.06.028 (2018).

442 5 Teesalu, T., Sugahara, K. N., Kotamraju, V. R. & Ruoslahti, E. C-end rule peptides mediate
443 neuropilin-1-dependent cell, vascular, and tissue penetration. *Proc Natl Acad Sci U S A*
444 **106**, 16157-16162, doi:10.1073/pnas.0908201106 (2009).

445 6 Tsai, Y. C. *et al.* Structural studies of neuropilin-2 reveal a zinc ion binding site remote
446 from the vascular endothelial growth factor binding pocket. *FEBS J* **283**, 1921-1934,
447 doi:10.1111/febs.13711 (2016).

448 7 Cannon, M. J., Schmid, D. S. & Hyde, T. B. Review of cytomegalovirus seroprevalence
449 and demographic characteristics associated with infection. *Rev Med Virol* **20**, 202-213,
450 doi:10.1002/rmv.655 (2010).

451 8 Ahlfors, K., Forsgren, M., Ivarsson, S. A., Harris, S. & Svanberg, L. Congenital
452 cytomegalovirus infection: on the relation between type and time of maternal infection
453 and infant's symptoms. *Scand J Infect Dis* **15**, 129-138, doi:10.3109/inf.1983.15.issue-
454 2.01 (1983).

455 9 Pass, R. F., Fowler, K. B., Boppana, S. B., Britt, W. J. & Stagno, S. Congenital
456 cytomegalovirus infection following first trimester maternal infection: symptoms at
457 birth and outcome. *J Clin Virol* **35**, 216-220, doi:10.1016/j.jcv.2005.09.015 (2006).

458 10 Roark, H. K., Jenks, J. A., Permar, S. R. & Schleiss, M. R. Animal Models of Congenital
459 Cytomegalovirus Transmission: Implications for Vaccine Development. *J Infect Dis* **221**,
460 S60-S73, doi:10.1093/infdis/jiz484 (2020).

461 11 Ligat, G., Cazal, R., Hantz, S. & Alain, S. The human cytomegalovirus terminase complex
462 as an antiviral target: a close-up view. *FEMS Microbiol Rev* **42**, 137-145,
463 doi:10.1093/femsre/fuy004 (2018).

464 12 Mumtaz, K. *et al.* Universal prophylaxis or preemptive strategy for cytomegalovirus
465 disease after liver transplantation: a systematic review and meta-analysis. *Am J*
466 *Transplant* **15**, 472-481, doi:10.1111/ajt.13044 (2015).

467 13 McGeoch, D. J., Cook, S., Dolan, A., Jamieson, F. E. & Telford, E. A. Molecular phylogeny
468 and evolutionary timescale for the family of mammalian herpesviruses. *J Mol Biol* **247**,
469 443-458, doi:10.1006/jmbi.1995.0152 (1995).

470 14 Isaacson, M. K. & Compton, T. Human cytomegalovirus glycoprotein B is required for
471 virus entry and cell-to-cell spread but not for virion attachment, assembly, or egress. *J*
472 *Virol* **83**, 3891-3903, doi:10.1128/JVI.01251-08 (2009).

473 15 Wang, D. & Shenk, T. Human cytomegalovirus virion protein complex required for
474 epithelial and endothelial cell tropism. *Proc Natl Acad Sci U S A* **102**, 18153-18158,
475 doi:10.1073/pnas.0509201102 (2005).

476 16 Zhou, M., Lanchy, J. M. & Ryckman, B. J. Human Cytomegalovirus gH/gL/gO Promotes
477 the Fusion Step of Entry into All Cell Types, whereas gH/gL/UL128-131 Broadens Virus
478 Tropism through a Distinct Mechanism. *J Virol* **89**, 8999-9009, doi:10.1128/JVI.01325-15
479 (2015).

480 17 Ciferri, C. *et al.* Structural and biochemical studies of HCMV gH/gL/gO and Pentamer
481 reveal mutually exclusive cell entry complexes. *Proc Natl Acad Sci U S A* **112**, 1767-1772,
482 doi:10.1073/pnas.1424818112 (2015).

483 18 Kabanova, A. *et al.* Platelet-derived growth factor-alpha receptor is the cellular receptor
484 for human cytomegalovirus gHgLgO trimer. *Nat Microbiol* **1**, 16082,
485 doi:10.1038/nmicrobiol.2016.82 (2016).

486 19 Wu, Y. *et al.* Human cytomegalovirus glycoprotein complex gH/gL/gO uses PDGFR-alpha
487 as a key for entry. *PLoS Pathog* **13**, e1006281, doi:10.1371/journal.ppat.1006281 (2017).

488 20 Kschonsak, M. *et al.* Structures of HCMV Trimer reveal the basis for receptor recognition
489 and cell entry. *Cell*, doi:10.1016/j.cell.2021.01.036 (2021).

490 21 Hahn, G. *et al.* Human cytomegalovirus UL131-128 genes are indispensable for virus
491 growth in endothelial cells and virus transfer to leukocytes. *J Virol* **78**, 10023-10033,
492 doi:10.1128/JVI.78.18.10023-10033.2004 (2004).

493 22 Ryckman, B. J. *et al.* Characterization of the human cytomegalovirus gH/gL/UL128-131
494 complex that mediates entry into epithelial and endothelial cells. *J Virol* **82**, 60-70,
495 doi:10.1128/JVI.01910-07 (2008).

496 23 Wille, P. T., Wisner, T. W., Ryckman, B. & Johnson, D. C. Human cytomegalovirus (HCMV)
497 glycoprotein gB promotes virus entry in trans acting as the viral fusion protein rather
498 than as a receptor-binding protein. *mBio* **4**, e00332-00313, doi:10.1128/mBio.00332-13
499 (2013).

500 24 Soker, S., Takashima, S., Miao, H. Q., Neufeld, G. & Klagsbrun, M. Neuropilin-1 is
501 expressed by endothelial and tumor cells as an isoform-specific receptor for vascular
502 endothelial growth factor. *Cell* **92**, 735-745, doi:10.1016/s0092-8674(00)81402-6 (1998).

503 25 Takagi, S., Tsuji, T., Amagai, T., Takamatsu, T. & Fujisawa, H. Specific cell surface labels in
504 the visual centers of *Xenopus laevis* tadpole identified using monoclonal antibodies. *Dev*
505 *Biol* **122**, 90-100, doi:10.1016/0012-1606(87)90335-6 (1987).

506 26 Dallas, N. A. *et al.* Neuropilin-2-mediated tumor growth and angiogenesis in pancreatic
507 adenocarcinoma. *Clin Cancer Res* **14**, 8052-8060, doi:10.1158/1078-0432.CCR-08-1520
508 (2008).

509 27 Kitsukawa, T., Shimono, A., Kawakami, A., Kondoh, H. & Fujisawa, H. Overexpression of a
510 membrane protein, neuropilin, in chimeric mice causes anomalies in the cardiovascular
511 system, nervous system and limbs. *Development* **121**, 4309-4318 (1995).

512 28 Prahst, C. *et al.* Neuropilin-1-VEGFR-2 complexing requires the PDZ-binding domain of
513 neuropilin-1. *J Biol Chem* **283**, 25110-25114, doi:10.1074/jbc.C800137200 (2008).

514 29 Takagi, S. *et al.* The A5 antigen, a candidate for the neuronal recognition molecule, has
515 homologies to complement components and coagulation factors. *Neuron* **7**, 295-307,
516 doi:10.1016/0896-6273(91)90268-5 (1991).

517 30 Favier, B. *et al.* Neuropilin-2 interacts with VEGFR-2 and VEGFR-3 and promotes human
518 endothelial cell survival and migration. *Blood* **108**, 1243-1250, doi:10.1182/blood-2005-
519 11-4447 (2006).

520 31 Parker, M. W., Xu, P., Li, X. & Vander Kooi, C. W. Structural basis for selective vascular
521 endothelial growth factor-A (VEGF-A) binding to neuropilin-1. *J Biol Chem* **287**, 11082-
522 11089, doi:10.1074/jbc.M111.331140 (2012).

523 32 Daly, J. L. *et al.* Neuropilin-1 is a host factor for SARS-CoV-2 infection. *Science* **370**, 861-
524 865, doi:10.1126/science.abd3072 (2020).

525 33 E, X. *et al.* OR14I1 is a receptor for the human cytomegalovirus pentameric complex and
526 defines viral epithelial cell tropism. *Proc Natl Acad Sci U S A* **116**, 7043-7052,
527 doi:10.1073/pnas.1814850116 (2019).

528 34 Vanarsdall, A. L. *et al.* CD147 Promotes Entry of Pentamer-Expressing Human
529 Cytomegalovirus into Epithelial and Endothelial Cells. *mBio* **9**, doi:10.1128/mBio.00781-
530 18 (2018).

531 35 Ha, S. *et al.* Neutralization of Diverse Human Cytomegalovirus Strains Conferred by
532 Antibodies Targeting Viral gH/gL/pUL128-131 Pentameric Complex. *J Virol* **91**,
533 doi:10.1128/JVI.02033-16 (2017).

534 36 Vanarsdall, A. L. *et al.* HCMV trimer- and pentamer-specific antibodies synergize for
535 virus neutralization but do not correlate with congenital transmission. *Proc Natl Acad Sci*
536 *U S A* **116**, 3728-3733, doi:10.1073/pnas.1814835116 (2019).

537 37 Freed, D. C. *et al.* Pentameric complex of viral glycoprotein H is the primary target for
538 potent neutralization by a human cytomegalovirus vaccine. *Proc Natl Acad Sci U S A* **110**,
539 E4997-5005, doi:10.1073/pnas.1316517110 (2013).

540 38 Appleton, B. A. *et al.* Structural studies of neuropilin/antibody complexes provide
541 insights into semaphorin and VEGF binding. *EMBO J* **26**, 4902-4912,
542 doi:10.1038/sj.emboj.7601906 (2007).

543 39 Cohen-Dvashi, H., Kilimnik, I. & Diskin, R. Structural basis for receptor recognition by
544 Lujo virus. *Nat Microbiol* **3**, 1153-1160, doi:10.1038/s41564-018-0224-5 (2018).

545 40 Parker, M. W. *et al.* Structural basis for VEGF-C binding to neuropilin-2 and
546 sequestration by a soluble splice form. *Structure* **23**, 677-687,
547 doi:10.1016/j.str.2015.01.018 (2015).

548 41 Vander Kooi, C. W. *et al.* Structural basis for ligand and heparin binding to neuropilin B
549 domains. *Proc Natl Acad Sci U S A* **104**, 6152-6157, doi:10.1073/pnas.0700043104
550 (2007).

551 42 Chandramouli, S. *et al.* Structural basis for potent antibody-mediated neutralization of
552 human cytomegalovirus. *Sci Immunol* **2**, doi:10.1126/sciimmunol.aan1457 (2017).

553 43 Xia, L. *et al.* Active evolution of memory B-cells specific to viral gH/gL/pUL128/130/131
554 pentameric complex in healthy subjects with silent human cytomegalovirus infection.
555 *Oncotarget* **8**, 73654-73669, doi:10.18632/oncotarget.18359 (2017).

556 44 Ye, X. *et al.* Recognition of a highly conserved glycoprotein B epitope by a bivalent
557 antibody neutralizing HCMV at a post-attachment step. *PLoS Pathog* **16**, e1008736,
558 doi:10.1371/journal.ppat.1008736 (2020).

559 45 Yelland, T. & Djordjevic, S. Crystal Structure of the Neuropilin-1 MAM Domain:
560 Completing the Neuropilin-1 Ectodomain Picture. *Structure* **24**, 2008-2015,
561 doi:10.1016/j.str.2016.08.017 (2016).

562 46 Sinzger, C. *et al.* Fibroblasts, epithelial cells, endothelial cells and smooth muscle cells
563 are major targets of human cytomegalovirus infection in lung and gastrointestinal
564 tissues. *J Gen Virol* **76 (Pt 4)**, 741-750, doi:10.1099/0022-1317-76-4-741 (1995).

565 47 Si, Z. *et al.* Different functional states of fusion protein gB revealed on human
566 cytomegalovirus by cryo electron tomography with Volta phase plate. *PLoS Pathog* **14**,
567 e1007452, doi:10.1371/journal.ppat.1007452 (2018).

568 48 Ciferri, C. *et al.* Antigenic Characterization of the HCMV gH/gL/gO and Pentamer Cell
569 Entry Complexes Reveals Binding Sites for Potently Neutralizing Human Antibodies. *PLoS*
570 *Pathog* **11**, e1005230, doi:10.1371/journal.ppat.1005230 (2015).

571 49 Gerna, G., Percivalle, E., Perez, L., Lanzavecchia, A. & Lilleri, D. Monoclonal Antibodies to
572 Different Components of the Human Cytomegalovirus (HCMV) Pentamer
573 gH/gL/pUL128L and Trimer gH/gL/gO as well as Antibodies Elicited during Primary
574 HCMV Infection Prevent Epithelial Cell Syncytium Formation. *J Virol* **90**, 6216-6223,
575 doi:10.1128/JVI.00121-16 (2016).

576 50 Su, H. *et al.* Potent Bispecific Neutralizing Antibody Targeting Glycoprotein B and the
577 gH/gL/pUL128/130/131 Complex of Human Cytomegalovirus. *Antimicrob Agents*
578 *Chemother* **65**, doi:10.1128/AAC.02422-20 (2021).

579 51 Jones, H. G. *et al.* Iterative screen optimization maximizes the efficiency of
580 macromolecular crystallization. *Acta Crystallogr F Struct Biol Commun* **75**, 123-131,
581 doi:10.1107/S2053230X18017338 (2019).

582 52 Battye, T. G., Kontogiannis, L., Johnson, O., Powell, H. R. & Leslie, A. G. iMOSFLM: a new
583 graphical interface for diffraction-image processing with MOSFLM. *Acta Crystallogr D*
584 *Biol Crystallogr* **67**, 271-281, doi:10.1107/S0907444910048675 (2011).

585 53 Evans, P. R. & Murshudov, G. N. How good are my data and what is the resolution? *Acta*
586 *Crystallogr D Biol Crystallogr* **69**, 1204-1214, doi:10.1107/S0907444913000061 (2013).

587 54 McCoy, A. J. Solving structures of protein complexes by molecular replacement with
588 Phaser. *Acta Crystallogr D Biol Crystallogr* **63**, 32-41, doi:10.1107/S0907444906045975
589 (2007).

590 55 Emsley, P. & Cowtan, K. Coot: model-building tools for molecular graphics. *Acta*
591 *Crystallogr D Biol Crystallogr* **60**, 2126-2132, doi:10.1107/S0907444904019158 (2004).

592 56 Adams, P. D. *et al.* PHENIX: building new software for automated crystallographic
593 structure determination. *Acta Crystallogr D Biol Crystallogr* **58**, 1948-1954,
594 doi:10.1107/s0907444902016657 (2002).

595 57 Croll, T. I. ISOLDE: a physically realistic environment for model building into low-
596 resolution electron-density maps. *Acta Crystallogr D Struct Biol* **74**, 519-530,
597 doi:10.1107/S2059798318002425 (2018).

598 58 Morin, A. *et al.* Collaboration gets the most out of software. *eLife* **2**, e01456,
599 doi:10.7554/eLife.01456 (2013).

600 59 Mastronarde, D. N. SerialEM: A Program for Automated Tilt Series Acquisition on Tecnai
601 Microscopes Using Prediction of Specimen Position. *Microscopy and Microanalysis*,
602 doi:10.1017/S1431927603445911 (2003).

603 60 Carragher, B. *et al.* Leginon: an automated system for acquisition of images from
604 vitreous ice specimens. *J Struct Biol* **132**, 33-45, doi:10.1006/jsbi.2000.4314 (2000).

605 61 Tegunov, D. & Cramer, P. Real-time cryo-electron microscopy data preprocessing with
606 Warp. *Nat Methods* **16**, 1146-1152, doi:10.1038/s41592-019-0580-y (2019).

607 62 Punjani, A., Rubinstein, J. L., Fleet, D. J. & Brubaker, M. A. cryoSPARC: algorithms for
608 rapid unsupervised cryo-EM structure determination. *Nat Methods* **14**, 290-296,
609 doi:10.1038/nmeth.4169 (2017).

610 63 Punjani, A., Zhang, H. & Fleet, D. J. Non-uniform refinement: adaptive regularization
611 improves single-particle cryo-EM reconstruction. *Nat Methods* **17**, 1214-1221,
612 doi:10.1038/s41592-020-00990-8 (2020).

613 64 Sanchez-Garcia, R. *et al.* DeepEMhancer: a deep learning solution for cryo-EM volume
614 post-processing. *bioRxiv*, doi:<https://doi.org/10.1101/2020.06.12.148296> (2020).

615 65 Pettersen, E. F. *et al.* UCSF Chimera--a visualization system for exploratory research and
616 analysis. *J Comput Chem* **25**, 1605-1612, doi:10.1002/jcc.20084 (2004).

617 66 Li, L. *et al.* Potent neutralizing antibodies elicited by dengue vaccine in rhesus macaque
618 target diverse epitopes. *PLoS pathogens* **15**, e1007716,
619 doi:10.1371/journal.ppat.1007716 (2019).

620 67 Ye, X. *et al.* Structural Basis for Recognition of Human Enterovirus 71 by a Bivalent
621 Broadly Neutralizing Monoclonal Antibody. *PLoS pathogens* **12**, e1005454,
622 doi:10.1371/journal.ppat.1005454 (2016).

623 68 Tang, A. *et al.* A novel high-throughput neutralization assay for supporting clinical
624 evaluations of human cytomegalovirus vaccines. *Vaccine* **29**, 8350-8356,
625 doi:10.1016/j.vaccine.2011.08.086 (2011).

626 69 Ye, X. *et al.* Identification of adipocyte plasma membrane-associated protein as a novel
627 modulator of human cytomegalovirus infection. *PLoS pathogens* **15**, e1007914,
628 doi:10.1371/journal.ppat.1007914 (2019).

629

630

Figure 1

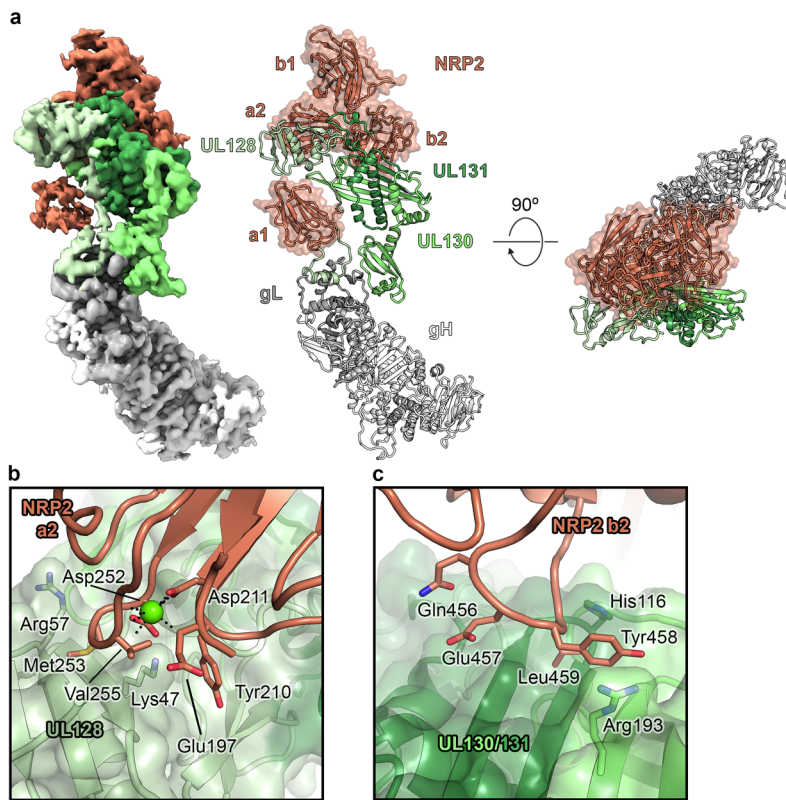


Figure 1: The cryo-EM structure of the HCMV Pentamer bound by NRP2. **(a)** Cryo-EM density is shown (left), with the Pentamer colored in shades of green, gray and white and NRP2 colored orange. The atomic model of this complex (right) is shown as ribbons, with the NRP2 also represented by a transparent molecular surface. **(b)** The interface between the NRP2 a2 domain and UL128. UL128 is depicted as a transparent, green molecular surface with ribbons underneath and NRP2 is shown as orange ribbons. Residues that are predicted to form critical contacts are shown as sticks. Oxygen, nitrogen, and sulfur atoms are colored red, blue, and yellow, respectively. The single calcium atom is shown as a bright green sphere, with black dotted lines depicting the interaction with conserved coordinating residues. **(c)** The interface between the NRP2 b2 domain and the HCMV Pentamer. ULs 130 and 131 are shown as a transparent, green molecular surface and NRP2 is shown as orange ribbons, with residues predicted to form critical contacts shown as sticks. Oxygen and nitrogen atoms are colored red and blue, respectively.

Figure 2

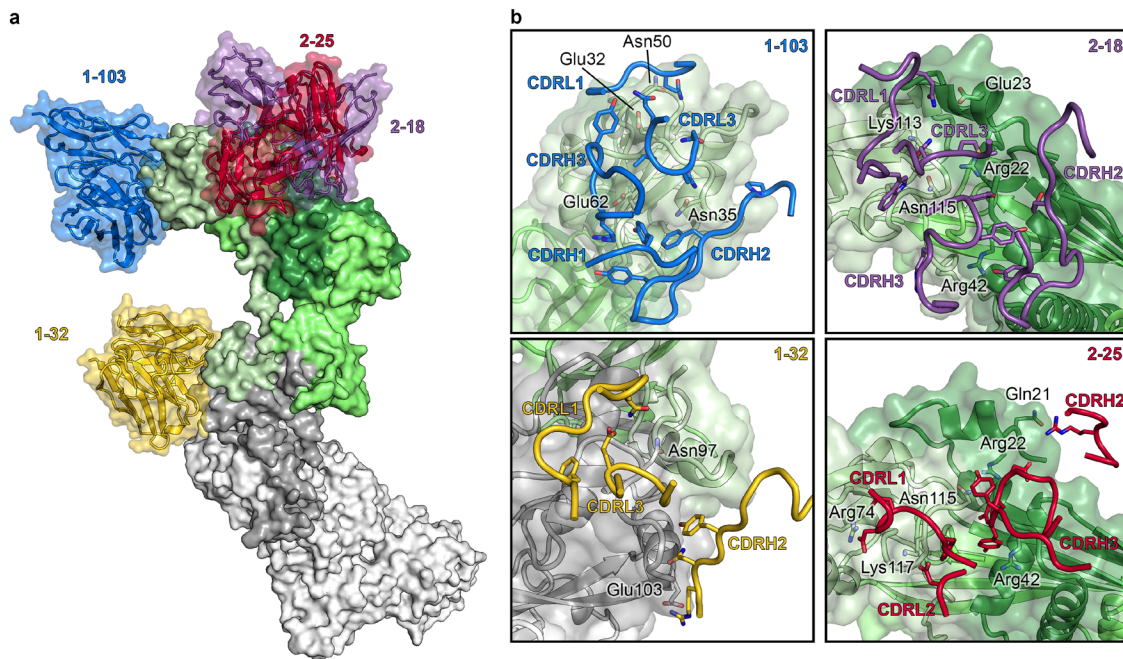


Figure 2: Composite of cryo-EM structures of Pentamer bound by four neutralizing human antibodies. **(a)** The atomic models of two cryo-EM structures of antibodies bound to the HCMV Pentamer are superimposed based on the position of the UL proteins. The Pentamer is shown as a molecular surface, colored according to **Fig. 1** and Fabs are shown as ribbons surrounded by a transparent molecular surface. Fab 1-103 is colored blue, Fab 1-32 is colored gold, Fab 2-18 is colored purple and Fab 2-25 is colored red. **(b)** CDRs from each Fab are shown as ribbons and the Pentamer is shown as a transparent, molecular surface with ribbons underneath. Predicted critical contact residues are shown as sticks. Fab 1-103 (*top left*) is colored blue, Fab 1-32 (*bottom left*) is colored gold, Fab 2-18 (*top right*) is colored purple and Fab 2-25 (*bottom right*) is colored red. Oxygen, nitrogen and sulfur atoms are colored red, blue and yellow respectively.

Figure 3

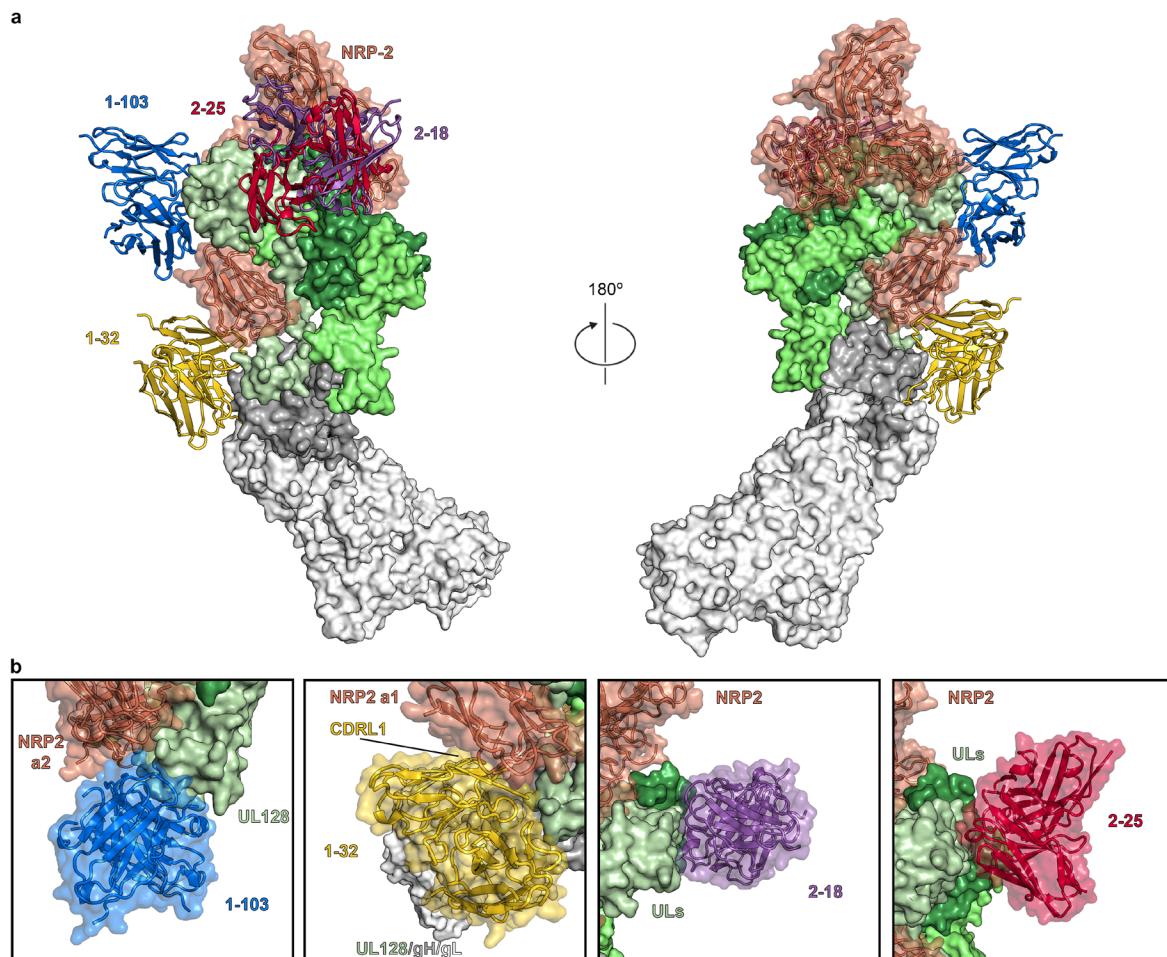


Figure 3: Pentamer-directed antibodies can neutralize HCMV via multiple mechanisms. **(a)** Cryo-EM structures of NRP2-bound Pentamer and Fab-bound Pentamer are superimposed based on the position of the UL proteins. Pentamer is shown as a molecular surface colored according to **Fig. 1**, Fabs are shown as ribbons, colored according to **Fig. 2**, and NRP2 is shown as orange ribbons surrounded by a transparent molecular surface. **(b)** Close-up views of each Fab-bound Pentamer are superimposed upon the NRP2-bound Pentamer. Both Fabs and NRP2 are shown as ribbons surrounded by a transparent molecular surface, while the Pentamer is shown as a solid molecular surface. NRP2 is colored orange, 1-103 is colored blue, 1-32 is colored gold, 2-18 is colored purple and 2-25 is colored red.

Figure 4

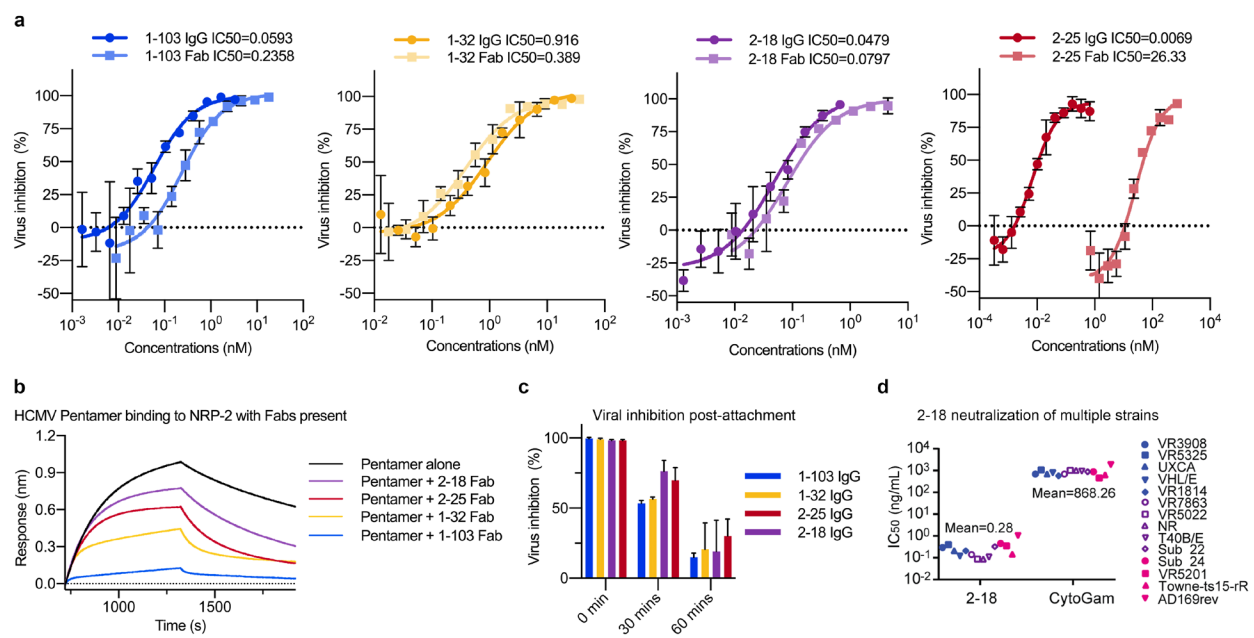
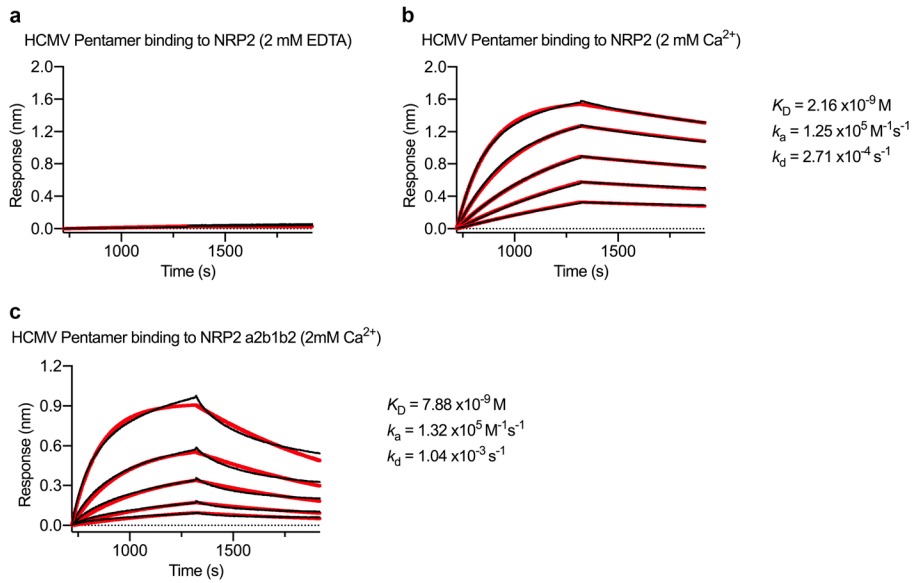


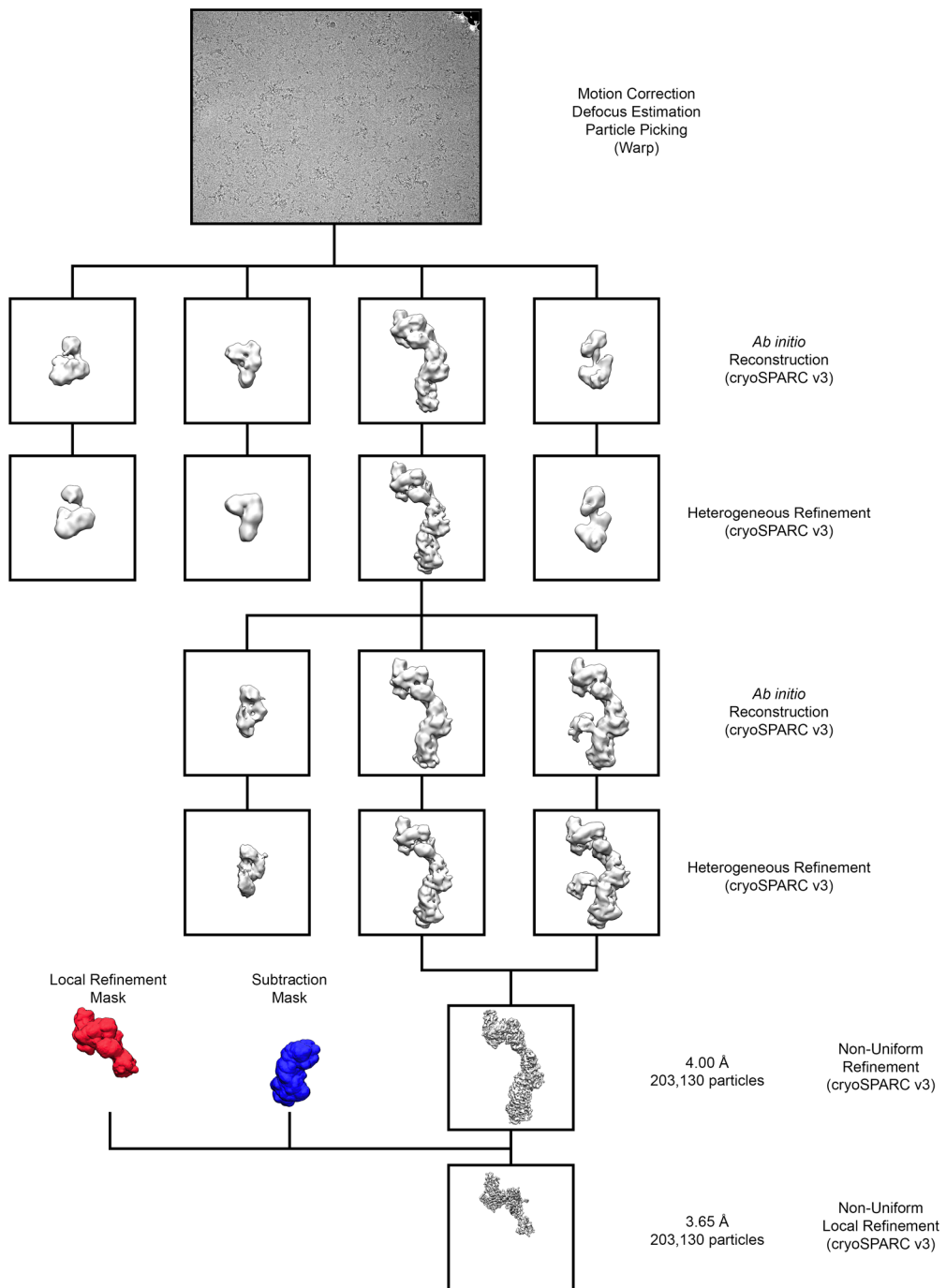
Figure 4: Antibodies 2-18 and 2-25 potently neutralize HCMV without disrupting NRP2 binding. **(a)** Neutralization curves are shown for each mAb based on inhibition of AD169rev-GFP infection in ARPE-19 cells. Inhibitory curves for both IgG and Fab are shown, with IgG shown in darker colors. **(b)** Sensorgrams from a BLI-based competition experiment are displayed. NRP2 was immobilized to a BLI sensor and dipped into Pentamer alone or Pentamer incubated with a molar excess of indicated Fab. **(c)** IgG neutralization of HCMV post-attachment to epithelial cells. AD169rev-GFP virions were allowed to adhere to ARPE-19 cells and saturating concentrations of IgG were added after a variety of different incubation periods. Viral inhibition is plotted for each IgG after either 0 mins incubation, 30 mins incubation, or 60 mins incubation. **(d)** Neutralization potency of 2-18 IgG was evaluated against twelve clinical isolates and two laboratory-adapted HCMV strains in ARPE-19 cells. IC₅₀ values were calculated by non-linear fit of the percentage of viral inhibition vs. concentration (ng/mL). The neutralization results of mAbs 1-103, 1-32 and 2-25 against the same panel of HCMV strains have been reported previously³⁵.

Supplementary Figure 1



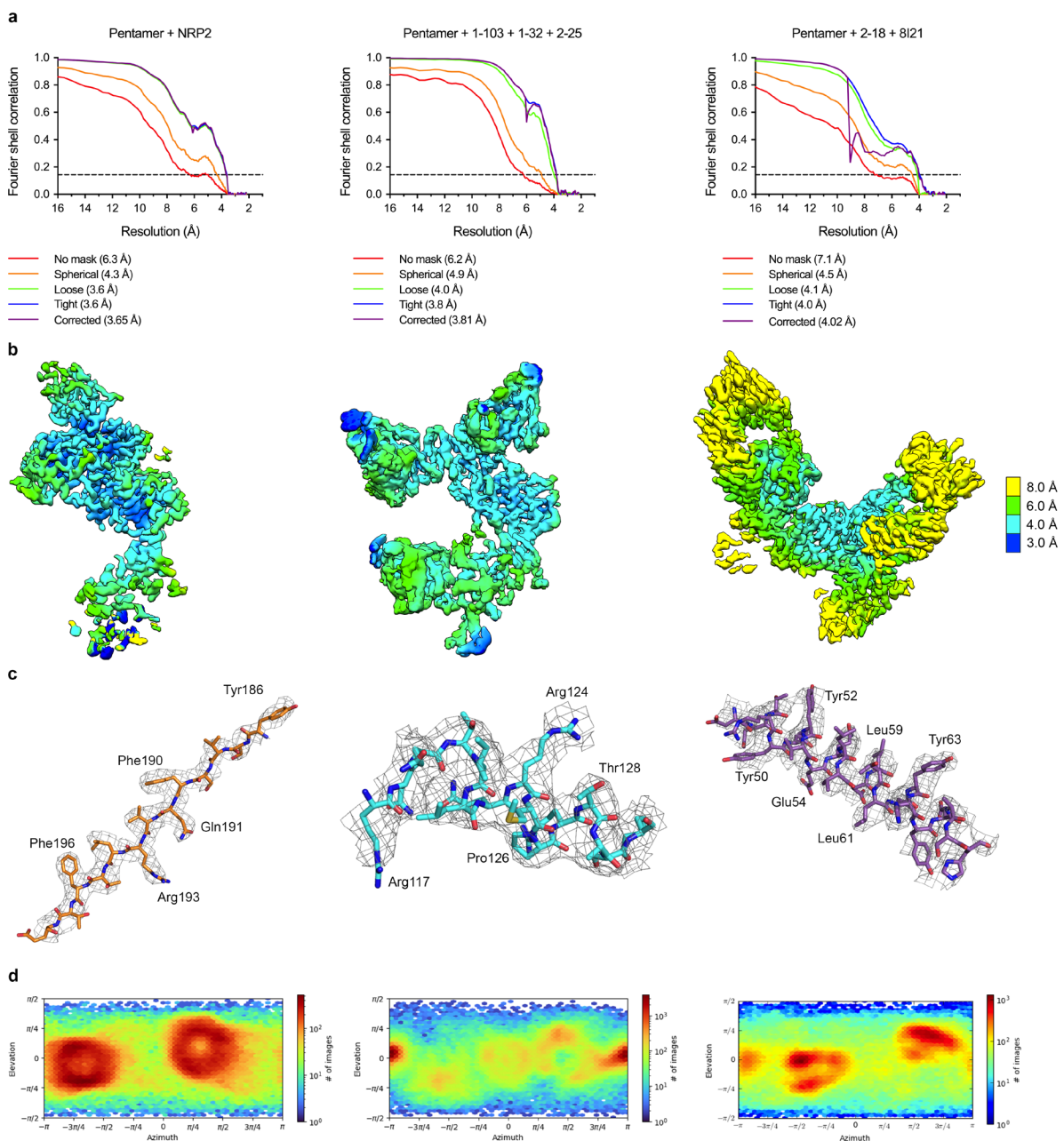
Supplementary Figure 1: The interaction between NRP2 and Pentamer is calcium-dependent. **(a)** BLI sensorgram showing the absence of binding between Pentamer and NRP2 in the presence of 2 mM EDTA. **(b)** BLI sensorgram showing binding between Pentamer and NRP2 in the presence of 2 mM calcium. Data are shown as black lines and best fit of a 1:1 binding model is shown as red lines. **(c)** BLI sensorgram showing binding between Pentamer and NRP2 a2b1b2 in the presence of 2 mM calcium. Data are shown as black lines and best fit of a 1:1 binding model is shown as red lines.

Supplementary Figure 2



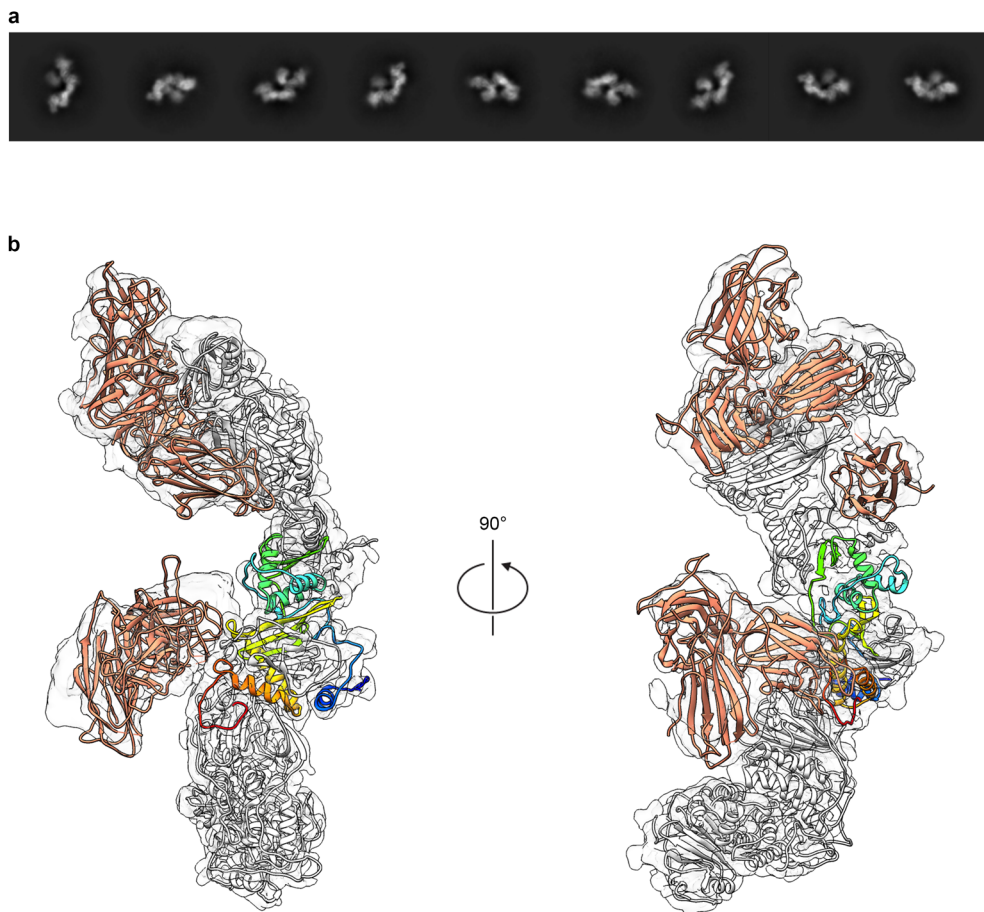
Supplementary Figure 2: Pentamer + NRP2 cryo-EM data processing workflow.

Supplementary Figure 3



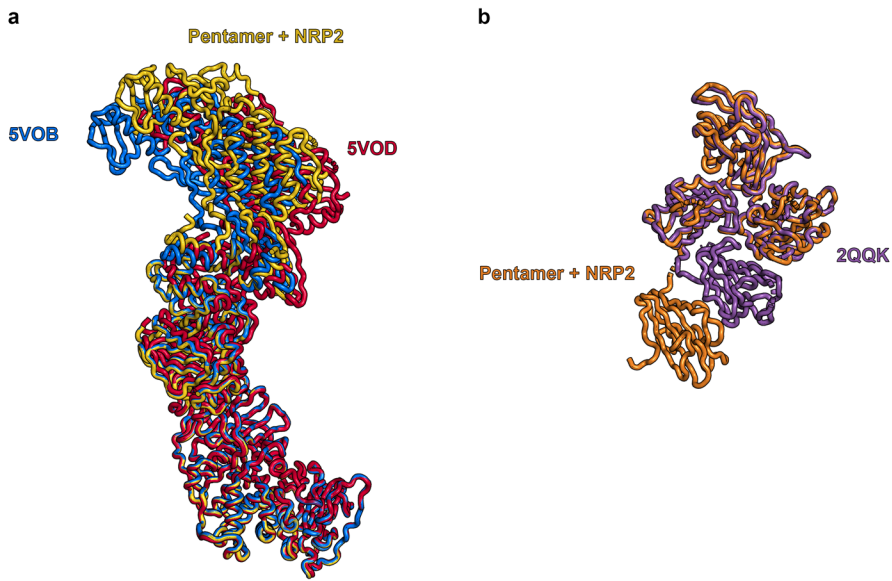
Supplementary Figure 3: Cryo-EM structure validation. **(a)** FSC curves are shown for focused refinements of Pentamer bound by NRP2 (*left*), Pentamer bound by 1-103, 1-32 and 2-25 (*middle*) and Pentamer bound by 2-18 and 8I21 (*right*). **(b)** Cryo-EM maps from each focused refinement are shown, colored according to local resolution. **(c)** Portions of each cryo-EM map are shown, with the corresponding atomic models docked into the density. Residue numbering corresponds to UL130 (*left, middle*) and UL131 (*right*). **(d)** Viewing Direction Distribution charts from cryoSPARC are shown for each focused refinement.

Supplementary Figure 4



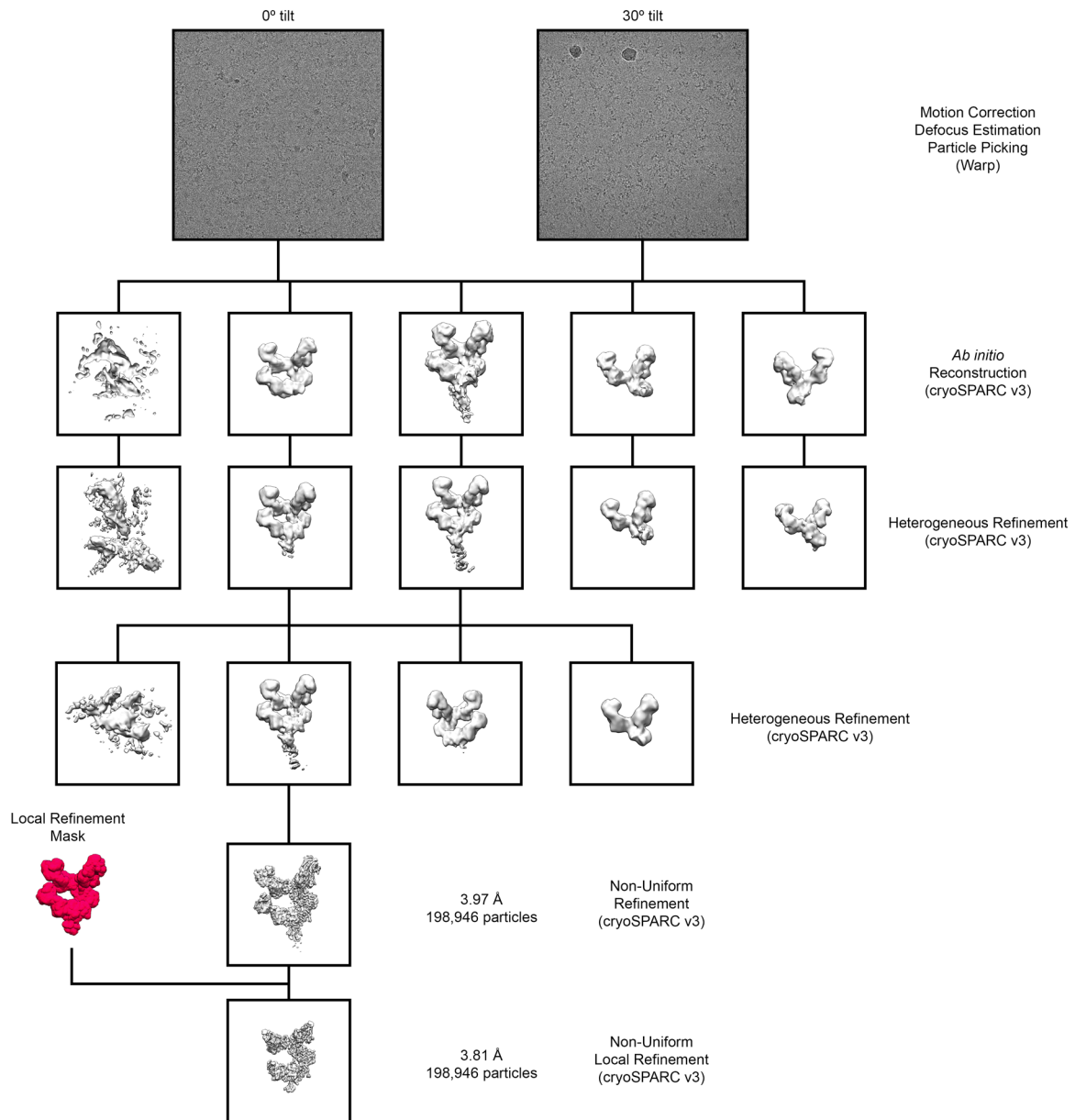
Supplementary Figure 4: A subset of particles display a second copy of NRP2 bound to the C-terminus of gL. **(a)** Two-dimensional class averages of Pentamer bound by two copies of NRP2 are shown. **(b)** A ~ 4.2 Å cryo-EM reconstruction of Pentamer bound by two copies of NRP2 is shown as a transparent surface. Atomic models of each component are docked in, shown as ribbons. Both copies of NRP2 are colored orange and Pentamer is colored white, except for gL, which is colored blue-to-red from the N-terminus to the C-terminus. The a1 domain from the gL-bound copy of NRP2 was excluded because it could not clearly be resolved in this reconstruction.

Supplementary Figure 5



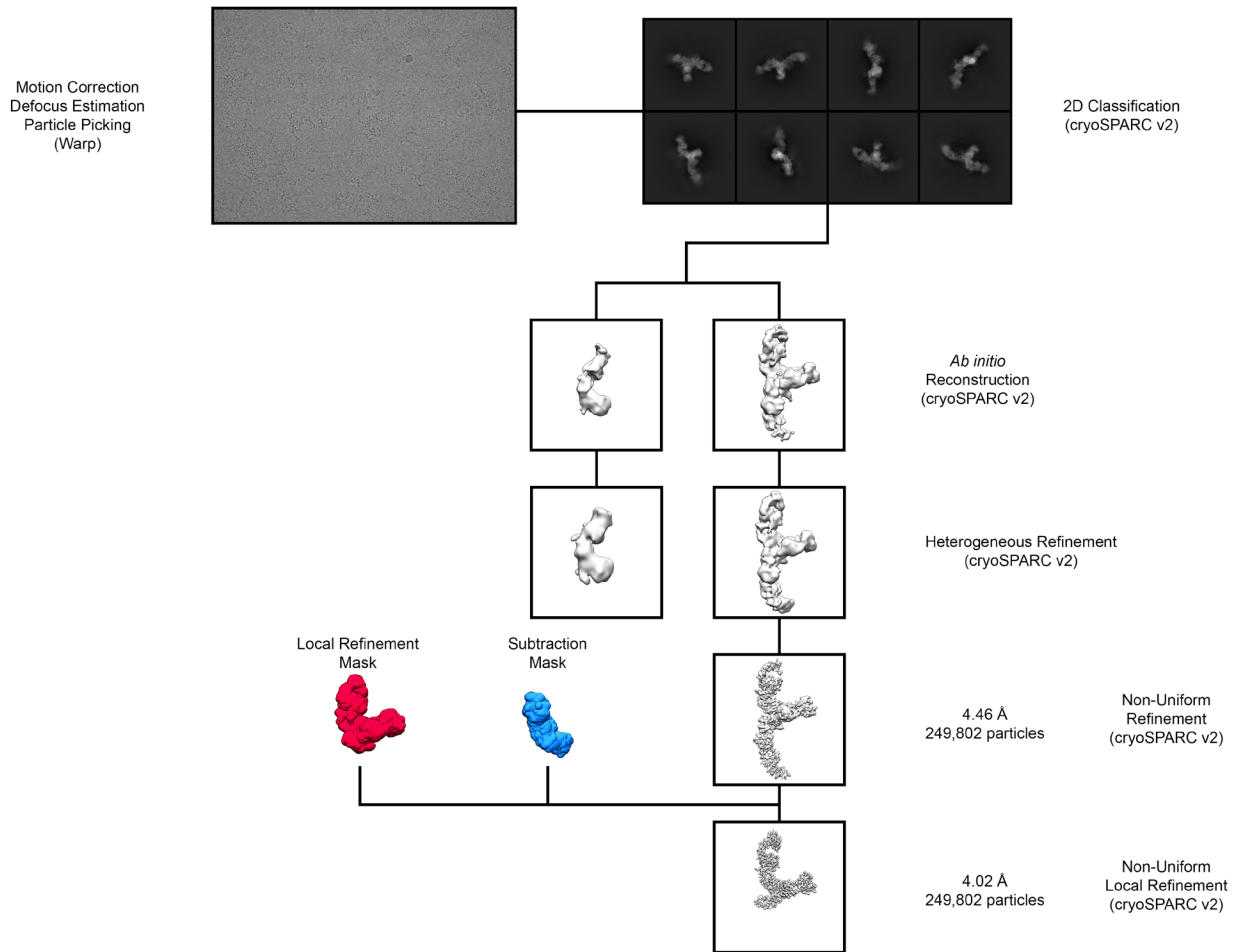
Supplementary Figure 5: NRP2 binding does not alter the conformation of Pentamer. **(a)** Previously reported crystal structures of Pentamer⁴² (PDB IDs: 5V0B and 5V0D) are aligned to the cryo-EM structure of the NRP2-bound Pentamer, based on the position of gH. 5V0B is colored blue, 5V0D is colored red and NRP2-bound Pentamer is colored yellow. **(b)** A previously reported crystal structure of NRP2³⁸ (PDB ID: 2QQK) is aligned to the cryo-EM structure of Pentamer-bound NRP2, based on the position of the b1 domain. 2QQK is colored purple and Pentamer-bound NRP2 is colored orange.

Supplementary Figure 6



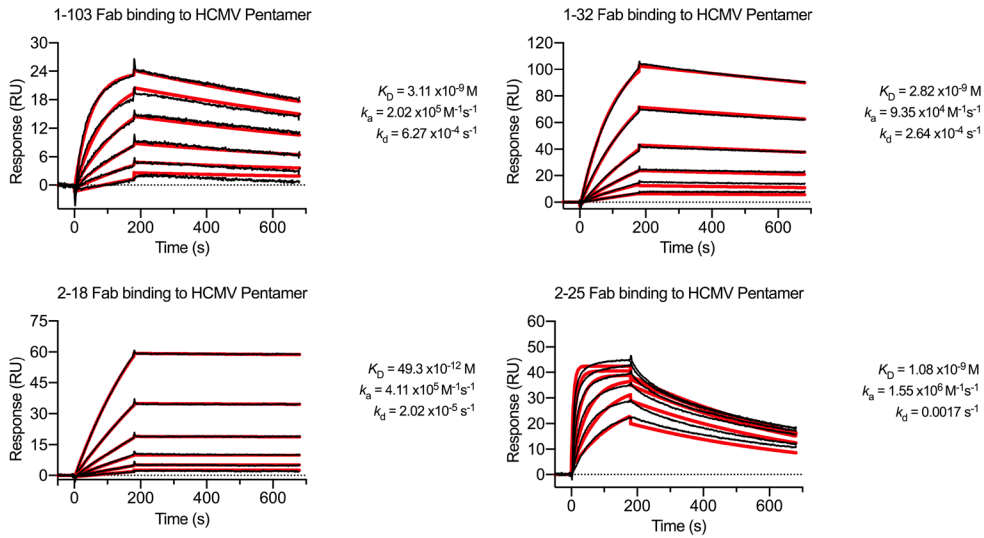
Supplementary Figure 6: Pentamer + 1-103 + 1-32 + 2-25 cryo-EM data processing workflow.

Supplementary Figure 7



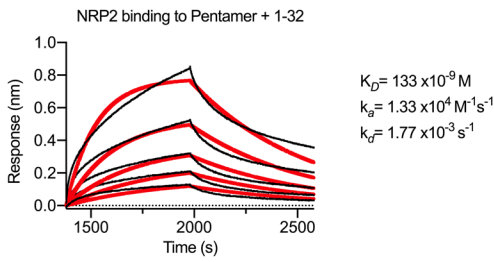
Supplementary Figure 7: Pentamer + 2-18 + 8I21 cryo-EM data processing workflow.

Supplementary Figure 8



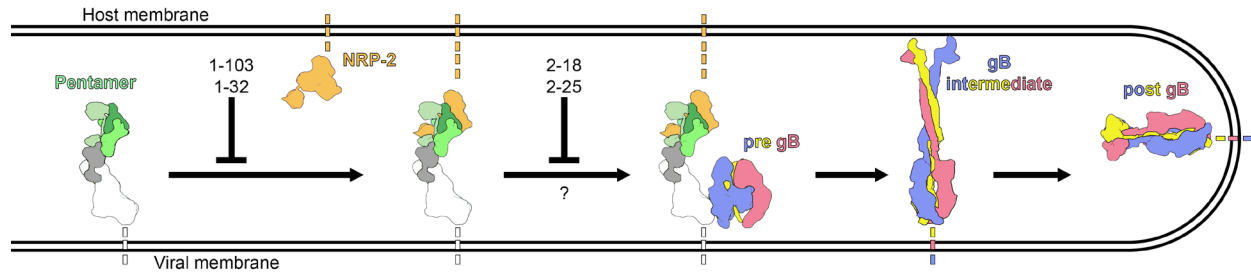
Supplementary Figure 8: Binding kinetics of Pentamer-directed antibodies. SPR sensorgrams showing binding of each of the four neutralizing Fabs are displayed, with data shown as black lines and the best fit of a 1:1 binding model shown as red lines.

Supplementary Figure 9



Supplementary Figure 9: NRP2 binding to Pentamer is partially disrupted by the presence of 1-32. Sensorgrams are shown for an experiment in which 1-32 IgG was immobilized to a BLI sensor, then used to capture Pentamer before being dipped into NRP2. Data for the association and dissociation of NRP2 are shown as black lines and the lines of best fit of a 1:1 binding model are shown as red lines.

Supplementary Figure 10



Supplementary Figure 10: Pentamer-directed mAbs neutralize via distinct mechanisms. A cartoon is shown depicting the infection of an endothelial or epithelial cell by HCMV. Pentamer is colored according to **Fig. 1**, NRP2 is colored orange and the three protomers of gB are colored red, blue and yellow. The stages of infection that mAbs 1-103, 1-32, 2-18 and 2-25 are predicted to disrupt are denoted by inhibition arrows.

Supplementary Table 1

	1-103 Fab	1-32 Fab	2-18 Fab	2-25 Fab
Data collection				
Facility	APS 19-ID	APS 19-ID	APS 19-ID	APS 19-ID
Wavelength (Å)	0.979	0.979	0.979	0.979
Space group	<i>P</i> 2	<i>P</i> 4 ₁ 2 ₁ 2	<i>C</i> 2	<i>P</i> 4 ₃ 2 ₁ 2
Cell dimensions				
<i>a</i> , <i>b</i> , <i>c</i> (Å)	95.4, 105.2, 102.7	65.7, 65.7, 191.9	129.5, 59.2, 141.7	180.9, 180.9, 138.9
α , β , γ (°)	90.0, 91.4, 90.0	90.0, 90.0, 90.0	90.0, 91.5, 90.0	90.0, 90.0, 90.0
Resolution range (Å)	52.62-1.90 (1.93-1.90)	54.20-2.10 (2.16-2.10)	65.02-2.80 (2.95-2.80)	69.89-2.51 (2.57-2.51)
R_{merge}	0.059 (0.407)	0.174 (0.951)	0.352 (1.283)	0.187 (2.033)
CC1/2	0.996 (0.736)	0.987 (0.753)	0.851 (0.291)	0.991 (0.522)
$I/\sigma I$	5.9 (1.8)	6.0 (1.5)	4.0 (1.7)	9.3 (2.0)
Completeness (%)	90.2 (91.3)	99.9 (99.8)	98.8 (96.7)	98.6 (99.9)
Redundancy	2.0 (2.0)	7.2 (6.6)	4.1 (3.8)	6.8 (7.1)
Refinement				
No. reflections	143,434 (14,383)	25,398 (2,476)	26,469 (2,446)	77,206 (7,680)
$R_{\text{work}}/R_{\text{free}}$ (%)	19.1/21.7	26.8/29.7	22.1/25.5	18.5/21.9
No. non-hydrogen atoms				
Protein	12,781	3,226	6,726	9,633
Ligand/ion	0	0	0	0
Water	1,627	70	70	507
B-factors (Å ²)				
Protein	28.7	62.9	27.0	39.9
Solvent	38.8	49.7	27.1	42.9
R.m.s. deviations				
Bond lengths (Å)	0.007	0.013	0.011	0.011
Bond angles (°)	1.33	1.41	1.46	1.23
Ramachandran (%)				
Favored	98.4	95.7	97.3	98.1
Allowed	1.6	4.3	2.7	1.9
Outliers	0	0	0	0
PDB ID	7LYV	7M1C	7KBA	7LYW

Supplementary Table 1: X-ray crystallographic data collection and refinement.

Supplementary Table 2

	Pentamer + NRP2	Pentamer + 2-18 + 8I21	Pentamer + 1-103 + 2-25 + 1-32
Data collection and processing			
Magnification (nominal)			
Voltage (kV)	300	300	300
Electron exposure (e/Å ²)	80	36	36
Defocus range (μm)	1.0-2.0	1.0-3.0	1.1-2.4
Pixel size (Å)	1.073	1.047	1.075
Symmetry imposed	n/a (C1)	n/a (C1)	n/a (C1)
Initial particles	745,025	1,489,510	834,092
Final particles	203,130	249,802	198,946
Map resolution (Å)	4.00	4.46	3.97
Focused refinement resolution (Å)	3.65	4.02	3.81
FSC threshold	0.143	0.143	0.143
Refinement			
Initial model(s) used (PDB ID)	5V0B, 2QQK	5V0B, 7KBA	5V0B, 7LYV, 7M1C, 7LYW
Model composition			
Protein atoms	6011	6422	9163
Protein B-factors (mean)	82.1	43.6	83.1
R.m.s. deviations			
Bond lengths (Å)	0.005	0.007	0.006
Bond angles (°)	1.14	1.38	1.38
Validation			
Molprobity score	1.69	2.21	1.84
Clashscore	7.47	14.42	8.91
Rotamer outliers (%)	0.61	1.58	0.89
Ramachandran plot			
Favored (%)	95.9	94.1	94.7
Allowed (%)	4.1	5.4	5.3
Outliers (%)	0.0	0.5	0.0
EMRinger score	2.84	1.21	1.80
Data Availability			
EMDB	23629	22788	23640
PDB	7M22	7KBB	7M30

Supplementary Table 2: Cryo-EM data collection and refinement.